



MARMARA UNIVERSITY
FACULTY OF ENGINEERING



INVESTIGATION OF EFFECT OF ACCUMULATORS SET IN AIR DUCTS IN FRONT PANEL OF AUTOMOBILE ON ENERGY EFFICIENCY

Abdullah KOÇAK

GRADUATION PROJECT REPORT
Department of Mechanical Engineering

Supervisor

Prof. Dr. Bülent EKİCİ

ISTANBUL, 2022



**MARMARA UNIVERSITY
FACULTY OF ENGINEERING**



**Investigation of Effect of Accumulators in Air Ducts in Front Panel of
Automobile on Energy Efficiency**

by

Abdullah KOÇAK

June 15, 2022, Istanbul

**SUBMITTED TO THE DEPARTMENT OF MECHANICAL ENGINEERING IN
PARTIAL FULFILLMENT OF THE REQUIREMENTS FOR THE DEGREE**

OF

BACHELOR OF SCIENCE

AT

MARMARA UNIVERSITY

The author(s) hereby grant(s) to Marmara University permission to reproduce and to distribute publicly paper and electronic copies of this document in whole or in part and declare that the prepared document does not in anyway include copying of previous work on the subject or the use of ideas, concepts, words, or structures regarding the subject without appropriate acknowledgement of the source material.

Signature of Author(s)
Department of Mechanical Engineering

Certified By

Project Supervisor, Department of Mechanical Engineering

Accepted By.....

Head of the Department of Mechanical Engineering

Acknowledgements

In the very first, I would like to acknowledge my supervisor, Prof. Dr. Bülent Ekici for his guidance, support and visionary knowedlege he provided me during my study. I would like to thank to him for encouraging and inspiring me by enthusiasm, erudition and useful advice that I am very grateful for the colloboration with Prof. Dr. Bülent Ekici. He guided me through the project patiently, made me have extreme perspectives during my research and gave me brilliant suggestions. Furthermore, I deeply appreciate the support from Arş.Gör. Murat Umut Yangaz whose advice enriched the my project. His guidance, expertise and rigorous attitude on the areas of fluid mechanics helpmed me refine my work on computational fluid dynamics (CFD) in this thesis.

I am also grateful to the academicds and students at the Marmara University, especially at the Faculty of Engineering. I always benefited from discussions with them, and they contributed a lot to my gaving a fullfilling Bachelor's Degree experience. I had amazing moments, knowledges and unforgettable fun in Marmara University. It was a home with full of nice people ,that are ready to help, for me.

Abstract

Electrical vehicles are in trend to take place of internal combustion vehicles with improving technologies in mean of electrical batteries, car mechanics and artificial intelligence. It is believed that electrical vehicles will be more popular in years without drivers. Moreover, an electrical vehicle provides a new opportunity for renewable energy. As it's main power is electricity, it is easier to implement an electric harvester on it for renewable energy.

This thesis describes how to conduct a wind energy harvester in car body to use wind occurs when car moves with average speeds. This structure should be well designed to avoid drag coefficient problems and also should produce enough energy to support car battery.

CFD simulations are essential here. It will help to understand which design is more suitable, how much energy the turbine will produce, what kind of improvements can be done and so on. The model only be in ANSYS software and analyzed there, there will be no prototype in real life to see real life results. The model captures air flow as car moves to use it to convert to turbine power then to electrical energy. It is a complicated process and should be efficient. By ANSYS Fluent analysis, the airduct in middle does not have a crucial affect on drag and lift coefficients, it can be located in middle with a bigger hole instead of thin pipelines in sides that will have less effective to produce energy as turbine would be thinner in thin pipeline.

Turbine geometry is analyzed deeply as it is the main component of energy harvesting. Horizontal axis wind turbines are more likely to produce high energy in more efficient way. However, they make a lot noise that is a big concern in social life as if there will be a lot turbined supported electrical vehicles. Moreover, in small sizes, vertical axis wind turbines can be more efficient as it does not get affected by wind direction, can produce energy in any direction. Plus, they have less lifetime cost so that they are commercially easier for drivers to deal with.

Lay Summary

Climate change mitigation is vitally important for all nations in the world. A key approach to replacing fossil fuels as an energy source and limiting carbon release is to invest in renewable energy technology. Wind energy is an attractive option regarding sustainable electricity. Vehicle Mounted Wind Turbine (VMWT) is a mounted horizontal axis wind turbine system for vehicles. VMWT has several smart features including high rpm turbine, convenient weight, practical shape and portability.

This thesis describes how effective can be to use vertical wind turbine mounted in air duct of an electrical vehicle to produce electrical energy.

Contents

Acknowledgements.....	i
Abstract.....	ii
Lay Summary.....	iii
Figures.....	vi
Tables.....	viii
Nomenclature.....	ix
Chapter 1: Introduction and Literature Review.....	1
1.1 Introduction.....	1
1.2 Wind Energy.....	3
1.3 Wind Turbines.....	5
1.3.1 Horizontal Axis Wind Turbines (HAWTs).....	5
1.3.2 Vertical Axis Wind Turbines (VAWTs).....	6
1.3.3 Savonius Turbines.....	7
1.3.3.1 Performance of Savonius Turbines.....	9
1.3.3.2 Parameters that affect the performance of Savonius wind turbine.....	10
i. Effect of blades number.....	10
ii. Effect of Aspect Ratio.....	10
ii. Effect of Overlap Ratio.....	11
Chapter 2: Mathematical Model.....	12
2.1 Introduction.....	12
2.2 Governing Equations.....	12
2.2.1 Continuity Equation.....	12
2.2.2 Momentum Equation.....	13
2.2.3 Energy Equation.....	18
2.2.4 Boundary Conditions.....	18
Chapter 3: Car Aerodynamics.....	20
3.1 History.....	20
3.2 Flow Around a Car.....	23
3.2.1 Drag and Lift.....	25
3.3 Drag Coefficient.....	25

3.4 Ground Effect.....	26
Chapter 4: Geometry Selections and ANSYS Analysis.....	27
4.1 Vehicle Selection.....	27
4.2 Air Duct Design 1.	31
4.3 Air Duct Design 2	36
4.4 Air Duct Design 3.....	39
4.5 Turbine Selection.....	42
4.6 Drag Force-Energy Analyzes with Turbines.....	44
4.6.1 Drag Force on Design 1 With Turbines.....	44
4.6.2 Drag Force on Design 2 With Turbines.....	46
4.7 Results.....	48
Chapter 5: Cost-Design Analysis and Conclusions.....	50
5.1 Cost-Design Analysis.....	50
5.2 Conclusion.....	51
References.....	53

Figures

Figure 1.1 Charles Brush's giant windmill for electricity generation, built in 1887–1888 (Windpower, 2003).

Figure 1.2 Illustration of the lift and drag forces acting on an airfoil blade.

Figure 1.3 Top view of savonius turbine

Figure 1.4 (a) Savonius wind turbine; (b)Top view and principle of Savonius rotor (Mathew, 2007)

Figure 1.5 (a) Two bladed savonius rotor (b) Conventional savonius rotor performance

Figure 2.1 (a) Infinitesimally small, moving control volume dV ; and (b) notation for stresses in the xy plane (Viola, 2018).

Figure 2.2 Shear stress tensor and pressure (Viola, 2018)

Figure 2.3 Elemental Cartesian fixed control volume showing surface force components in the x -direction only (Anderson, 2009)

Figure 3.1 Comparison of a plane wing profile and evolution of cars.

Figure 3.2 First prototypes of cars based in planes and ships forms (Jamais Contente and Alfa Romeo of 1914)

Figure 3.3 Jaray's Design

Figure 3.4 A is frontal area; b is wide; h is height

Figure 3.5 Mercerdes-Benz CLA which CD is 0.23

Figure 4.1 Tesla Cyber Truck

Figure 4.2 Dimensions of Cyber Truck

Figure 4.3 Cybertruck drawn in SolidWorks

Figure 4.4 Technical Drawing of selected vehicle

Figure 4.5 Mesh Structure of the vehicle

Figure 4.6 Figure 4.6 Mesh Properties of Simulation 1

Figure 4.7 Boundary conditions of Simulation 1

Figure 4.8 Drag coefficient by iteration taken from ANSYS Report

Figure 4.9 Drag force and drag coefficinet calculated by ANSYS Software

Figure 4.10 (a) Front view of Design 1 **(b)** Section view of Design 1

Figure 4.11 Technical Drawing of Design 1

Figure 4.12 Meshig of Design 1

Figure 4.13 Mesh quality of design 1

Figure 4.14 Boundary conditions of Simulation 2

Figure 4.15 Drag coefficient by iteration taken from ANSYS Report

Figure 4.16 Drag coefficient and force applied on vehicle design 1

Figure 4.17 (a) Front view of Design 2 **(b)** Section view of Design 2

Figure 4.18 Technical Drawing of Design 2

Figure 4.19 Meshing of Design 2

Figure 4.20 Mesh Quality of design 2

Figure 4.21 Drag coefficient by iteration taken from ANSYS Report

Figure 4.22 Drag coefficient and force applied on vehicle design 2

Figure 4.23 Design 3

Figure 4.24 Technical Drawing of Design 3.

Figure 4.25 Quality of Meshing

Figure 4.26 Drag Force plot taken form ANSYS Report

Figure 4.27 Drag force and drag coefficinet of Design 3

Figure 4.28 (a) 2-Blade Savonius turbine **(b)** Technical drawing

Figure 4.29 Wind Turbines set in front panel

Figure 4.30 Drag force applied on design 1 with set of air ducts

Figure 4.31 Drag force and coefficient simulated by ANSYS at 90km/hr speed

Figure 4.32 Wind Turbines set in middle of front panel

Figure 4.33 Drag force acting on vehicle body at 90 km/hr speed.

Figure 4.34 Drag force and coefficient simulated by ANSYS at 90km/hr speed

Tables

Table 4.1 Correlation of variables with Car Speed

Table 4.2 Solver Parameters

Table 4.3 Boundary Conditions

Table 4.4 Data of coefficients

Nomenclature

\vec{C}_L, \vec{C}_D	Lift and drag coefficients
\vec{e}_L, \vec{e}_D	Unit vectors in lift and drag coefficients
\vec{f}_L, \vec{f}_{Li}	Lift component per unit span on the i^{th} blade (N/m)
\vec{f}_D, \vec{f}_{Di}	Drag component per unit span on the i^{th} blade (N/m)
\vec{F}_L, \vec{F}_D	Turbine lift and drag forces per unit span (N/m)
\vec{F}_t, \vec{F}_n	Tangential and normal forces per unit span (N/m)
\vec{F}_x, \vec{F}_y	Body forces per unit span in x- and y- axis directions
L	Blade length (m)
M	Blade mass per unit span (kg/m)
r	Radial distance from the rotor center (m)
u, v, w	Three components of local velocity (m/s)
(x, y, z)	Coordinates in the original reference frame (m)
ρ	Fluid density ($\frac{kg}{m^3}$)

Chapter 1

Introduction and Literature Review

This chapter provides a brief introduction to renewable wind and tidal energy, with the main focus on present-day tidal stream turbine technology. Various computational fluid dynamics (CFD) techniques are then reviewed, leading to the aim and objectives of this thesis. The chapter concludes with a synopsis and list of publications.

1.1 Introduction

Alternative energy vehicles, such as solar-powered, hybrid, and plug-in hybrid vehicles, are becoming increasingly popular. Electric automobiles are gradually displacing gasoline-powered vehicles. Internal combustion engines produce a great deal of pollution. It is at this point that the need for entirely sustainable and pollution-free energy-powered cars emerges. Wind energy is free, renewable, unlimited, and abundant in the atmosphere. China is the world's greatest wind energy generator, with 145,362 MW. Asia is the fastest expanding region in terms of wind energy. A wind turbine is a device that uses a generator to transform the kinetic energy of the wind into mechanical energy and then into electricity.[1]

Academics and governments are both interested in the development of renewable energy systems. It would not only provide an almost limitless source of energy, but it would also help to safeguard the environment and human health by lowering emissions of greenhouse gases (CO₂), as well as hazardous nitrogen and sulphur compounds.

The application of wind energy to automobiles has significant implications for ecologically benign, long-term development. It complies with the 2015 Paris Agreement, which prioritizes renewable energy, as well as the European Union's 2030 Climate and Energy Framework.

It would assist to lessen reliance on traditional energy sources such as fossil fuels. The depletion of oil reserves as a result of increased global oil demand should also be emphasized. According to some scientists, oil supplies could be depleted in the next 40–60 years.

Charging the batteries while the vehicle is in motion can extend the range of electrically propelled vehicles. This can be accomplished by catching air currents and using them as a

source of energy. There are two types of wind resistance that act as a vehicle moves: frictional drag and form drag. Frictional drag is caused by air viscosity, while form drag is caused by differences in air pressure in the front and rear of the vehicle. We can capture energy from a stationary wind turbine positioned near a road when it rotates owing to air movement generated by automobiles passing by. If the wind streams can be captured within the vehicle, they can be used to recuperate some of the energy that was spent to overcome the vehicle's form drag. This method employs a wind turbine mounted in front of a vehicle that rotates and transforms kinetic energy into electrical energy via a generator. The chamber has a front air intake entrance and a back air departure vent. The noise produced by the wind turbine is reduced with sound-absorbing materials. This energy is stored in a battery separate from the vehicle's battery system. This, in turn, functions as a reservoir, increasing the vehicle's overall efficiency. The vehicle must be charged externally, just like a regular electric car, even though wind energy will help it later. The project's major goal is to conserve the planet Earth, which is in grave danger due to many sorts of pollution, primarily from growing and out-of-control cars, which produce emissions on a far bigger scale.

1.2 Wind Energy

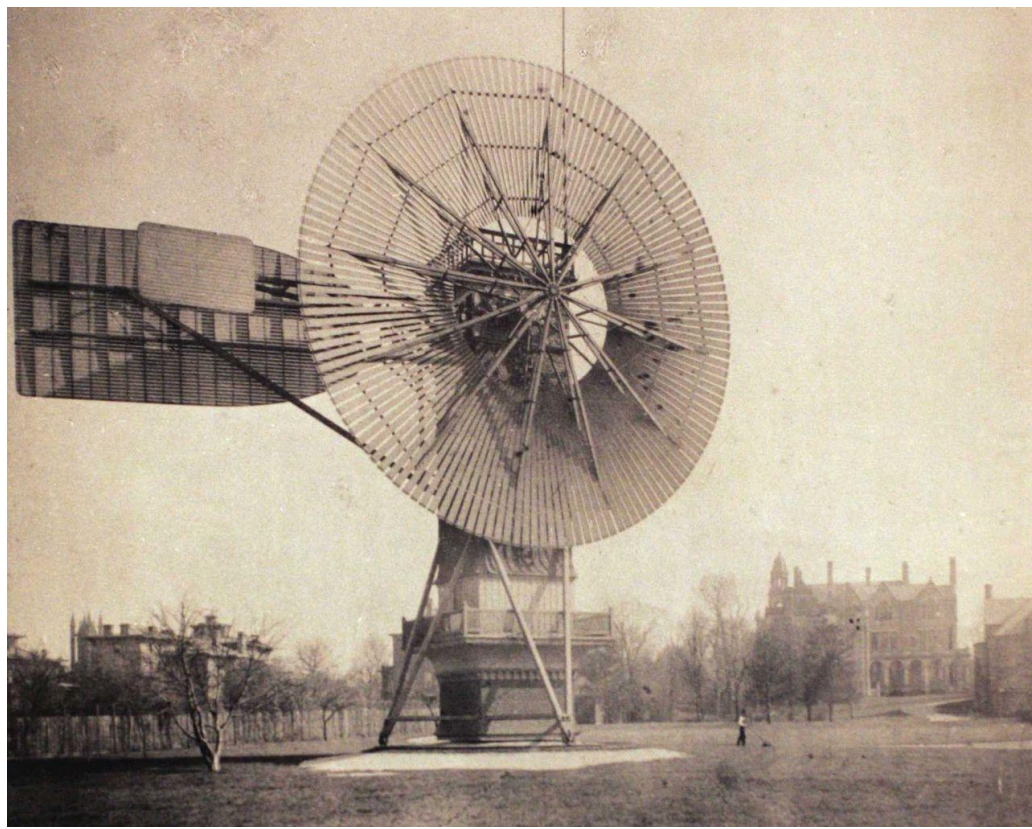


Figure 1.1 Charles Brush's giant windmill for electricity generation, built in 1887–1888 (Windpower, 2003).

Because of the global commitment to minimize GHG emissions while providing appropriate energy to various countries, renewables will play a critical part in the future energy supplement (Mathew, 2007). Wind has become one of the most commercially successful and cost-effective renewable energy sources in recent years (Mathew, 2007). Wind power has been employed since ancient times, when ships and boats were propelled by sails. In agriculture, wind power has been used in grain mills and water pumps (Dyachuk, 2015; cited by Mathew, 2007). The Persians built the first documented wind mills around two thousand years ago, and they were vertical-axis machines with reed or wooden sails. Europeans, utilizing horizontal-axis mills, established a similar technology by the 13th century (Dyachuk, 2015; cited in Mathew, 2007). Both the Scottish scientist and engineer James Blyth and the American engineer and inventor Charles Brush contributed significantly to the development of the first wind turbine in 1887. (Blyth, 1888; Price, 2005). The massive Brush windmill is depicted in Figure 1.1. After 1890, as rotors with low-solidity and aerodynamically constructed blades gained progressively spectacular performance in the field, more methodical approaches for turbine design were

employed (Mathew, 2006). The Savonius rotor, invented in Finland by Sigurd Johannes Savonius in the early 1920s and patented in the United States, consisted of a vertical-axis turbine driven by the drag force component from wind or flowing water (Savonius, 1929, 1930, 1931). The Darrieus turbine, created by a French aviation engineer Georges Jean Marie Darrieus and patented in the United States in 1931, was another vertical-axis turbine design (Ramler & Donovan, 1979). The Darrieus turbine is a lift-based rotor with a lift force component that generates most of the torque. It is more efficient than the Savonius turbine since it uses less material in its construction (Darrieus, 1931; Dyachuk, 2015). The following section delves deeper into these two types of vertical-axis turbines. During the 1950s, the notion of high tip-speed ratio and low-solidity turbines was introduced. Prior to the 1973 oil crisis, which triggered a revival in interest in renewable energy, cheaper and more reliable electricity from fossil fuel and nuclear power led a fall in interest in wind energy. The National Aeronautics and Space Administration (NASA) created a succession of horizontal-axis wind turbines with US government backing until the mid-1980s, following research on resource analysis, hardware development, and cost-cutting approaches (Johnson, 2001; Mathew, 2007). From the 1970s through the early 1990s, scientists at Sandia Laboratories concentrated their efforts on the development of the Darrieus turbine (Sheldahl & Blackwell, 1977). Several additional novel designs, such as the vortex turbine, diffuser augmented design, and Musgrove rotor, were proposed at this time, with prototypes built and tested. Several businesses have produced horizontal- and vertical-axis wind turbines, with the horizontal-axis rotor type being the most successful (Mathew, 2007).

1.3 Wind Turbines

Numerous types and shapes of turbines have been built and developed around the world since the inception of wind generating technologies. However, only a few of the most inventive ideas have been commercially produced. The types of wind and tidal turbines are divided into horizontal- and vertical-axis machines in this thesis, based on their rotational axis.

1.3.1 Horizontal Axis Wind Turbines (HAWTs)

HAWTs are the most common wind machine designs in use today. HAWTs utilize aerodynamic blades (i.e. airfoils) fitted to a rotor, which can be positioned either upwind or downwind. HAWTs are typically either two- or three-bladed and operate at high blade tip speeds. Machines with upwind rotors require a yaw, or tail vane, to help them orient into the wind while downwind rotors have blades that are coned allowing the turbine to orient on its own. One drawback identified with downwind rotors, however, is that they have been known to ‘walk’ around when trying to line up with winds during low speed conditions, diminishing low wind speed energy production. The force of the lift is actually stronger than the force of the wind against the blade, or the drag, which acts in parallel with the airflows. This allows turbine blades to turn at speeds greater than could be achieved relying on drag forces alone. Although some wind turbines also use the drag force to produce energy, most HAWTs are designed to minimize drag while maximizing lift.

HAWTs work predominantly on lift principle. As the wind stream interacts with the rotor blades, lift force is generated as explained in the previous section, causing the rotor to rotate. The rotational speed varies with the design features and the size of the rotor. For a typical MW-sized turbine, this could be as low as 16 rpm. The low-speed main shaft transmits this rotation to the high-speed shaft through the gearbox (there are direct drive turbines also, which do not have a gearbox in the transmission line). The speed is enhanced by the gear trains to match with the higher speed requirement of the generator. The generator then converts the mechanical energy to electrical energy. There are a series of control systems in between for yaw alignment, power regulation, and safety.

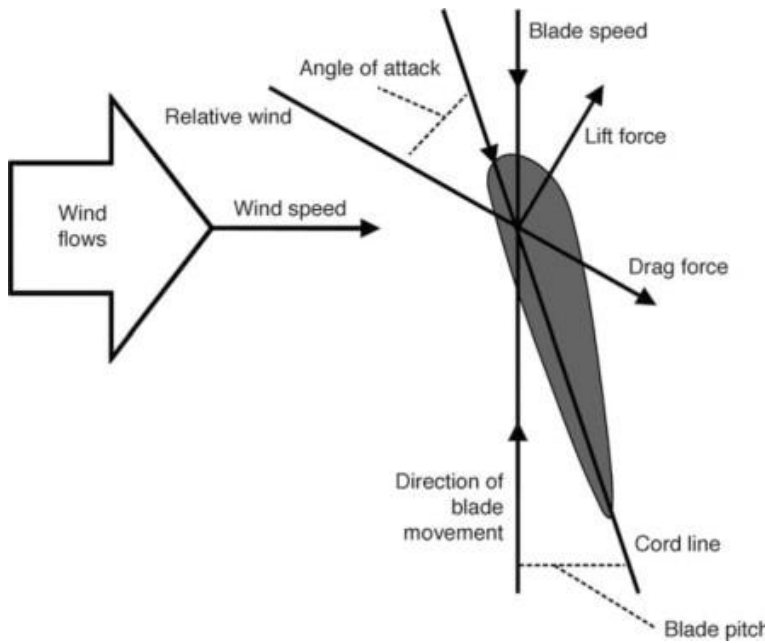


Figure 1.2 Illustration of the lift and drag forces acting on an airfoil blade.

The number of blades on a horizontal-axis turbine can be classed as single-bladed, two-bladed, three-bladed, or multi-bladed. Due to the stability of the relatively homogeneous aerodynamic loading, three-bladed turbines are the commercial equipment traditionally utilized for energy generation. Multi-bladed rotors have a high solidity (ratio of real blade area to swept turbine area) and can self-start, but only when not loaded (Mathew, 2007).

1.3.2 Vertical Axis Wind Turbines (VAWTs)

Vertical axis wind turbines (or VAWTs) have the main rotor shaft arranged vertically. Key advantages of this arrangement are that the turbine does not need to be pointed into the wind to be effective. This is an advantage on sites where the wind direction is highly variable. VAWTs can utilise winds from varying directions. With a vertical axis, the generator and gearbox can be placed near the ground, so the tower doesn't need to support it, and it is more accessible for maintenance. Drawbacks are that some designs produce pulsating torque. Drag may be created when the blade rotates into the wind.

In the VAWTs the main rotor shaft is placed in a transverse position to the wind. The main component of this type such as the generator and the gearbox are positioned near to the ground. This type is used in the sites where the wind is usually varying its direction because the rotors are always directed into the wind. There are two subtypes in the VAWTs, the darrieus, and

savonius wind turbines. Darrieus wind turbines are efficient but they require an additional power source to start the turbine rotation, and they may cause cyclic stress on the turbine tower. Savonius wind turbines do not require any external power source for the starting process, and they are frequently used in the areas where the turbulent wind occurs, and they are less efficient compared to darrieus wind turbines. The VAWTs have many advantages. For instance, they do not require any mechanisms to point the rotor blades toward the wind and the maintenance of the main parts is easier since they are close to the ground. Additionally, they are commonly utilized in the places where tall structures are not allowed, on mesas, and hilltops.

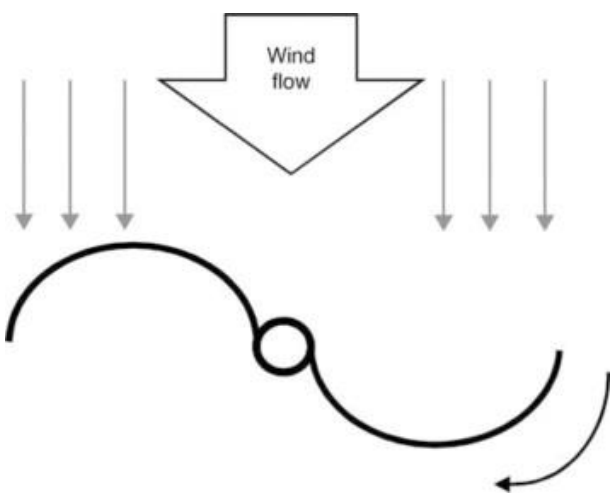


Figure 1.3 Top view of savonius turbine

The vertical axis wind turbine has a major advantage in the areas where the direction of the wind fluctuates significantly.

The gearboxes and generators of these turbines can position closer to the ground by driving them directly from the assembly of the rotor to the base's gearbox, increasing maintainability. The vertical axis wind turbine gearbox is much more fatigue as compared to gearboxes of other types of wind turbine. However, it has a major disadvantage is that this turbine generates low average energy compared to the horizontal axis wind turbine.

1.3.3 Savonius Turbine

Sigurd Johannes Savonius designed the Savonius wind turbine in 1922. It is a form of vertical-axis rotor. As illustrated in Figure 1.4, it comprises of two or three scoop blades placed in an S-shaped cross section (a). As seen in Figure 1.4, the convex side of one scoop and the concave side of the other scoop both face the flow at the same time (b). As a result, the Savonius turbine uses a drag-driving rotor, with the concave side having a higher drag coefficient than the convex

side. The Savonius turbine can accept flow from either direction and has a low cut-in speed; nevertheless, it is limited to a smaller number of applications due to its inefficiency at low tip speed ratios (Sahim et al., 2018).

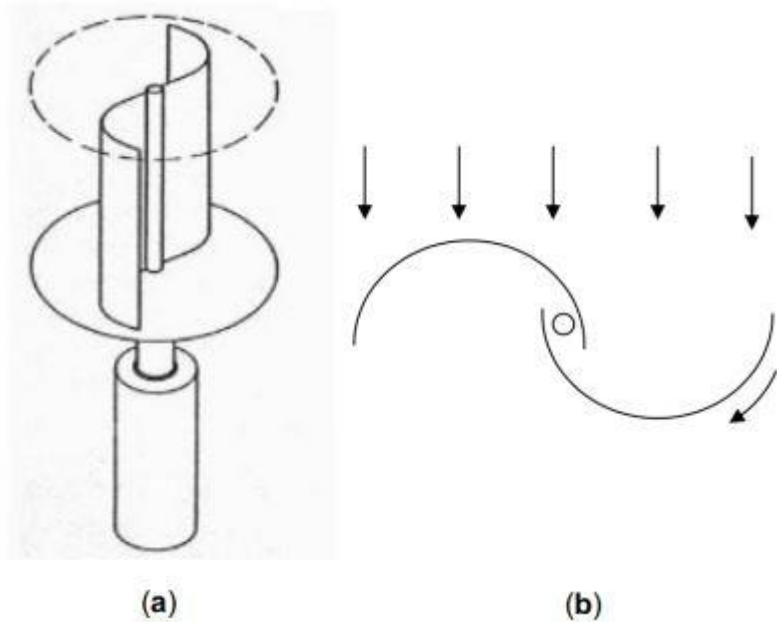


Figure 1.4 (a) Savonius wind turbine; (b)Top view and principle of Savonius rotor (Mathew, 2007)

The Savonius wind turbine is a simple vertical axis device having a shape of half-cylindrical parts attached to the opposite sides of a vertical shaft (for two-bladed arrangement) and operate on the drag force, so it can't rotate faster than the wind speed. This means that the tip speed ratio is equal to 1 or smaller .As the wind blows into the structure and comes into contact with the opposite faced surfaces (one convex and other concave), two different forces (drag and lift) are exerted on those two surfaces. The basic principle is based on the difference of the drag force between the convex and the concave parts of the rotor blades when they rotate around a vertical shaft. Thus, drag force is the main driving force of the savonius rotor . Fig.1.5(a) shows characteristic parameters of a savonius wind turbine with two semi circular profile blades.

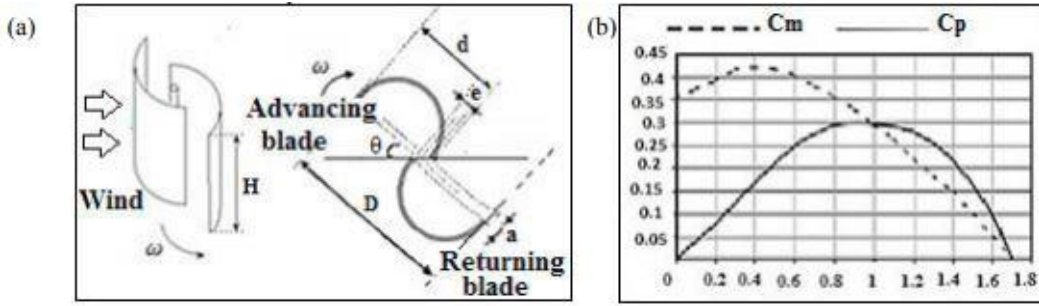


Figure 1.5 (a) Two bladed savonius rotor (b) Conventional savonius rotor performance

1.3.3.1 Performance of Savonius turbine

The performance of Savonius wind turbine can be expressed in the form of coefficient of power C_p Eq.(1.4) and torque coefficient C_m Eq.(1.5) in comparison with the tip speed ratio (TSR) λ Eq.(1.1). TSR is a ratio between the speed of tip blade and wind speed through the blade obtained by Eq.(1.1).

$$\lambda = \frac{V_{rotor}}{V} = \frac{\omega R}{V} \quad (1.1)$$

$$P_A = \text{Kinetic energy} * \text{mass flow rate} = \frac{1}{2} V^2 \rho S V \quad (1.2)$$

$$P_T = T \omega \quad (1.3)$$

$$C_p = \frac{P_T}{P_A} \quad (1.4)$$

$$C_m = \frac{T}{T_W} \quad (1.5)$$

Conventional Savonius rotor is a rotor with the geometrical parameters a and e are respectively equal to 0 and $D/6$. This rotor has been largely studied. The values of C_p and C_m are experimentally determined as a function of the velocity coefficient λ , Fig.1

1.3.3.2 Parameters that affect the performance of Savonius wind turbine

i. Effect of blades number

The number of blades have an important impact in the rotor's performance. It is concluded that the optimum number of blades is two for the Savonius rotor whether it is single, two or three stage, also that the two blades Savonius wind turbine is more efficient, it has higher power coefficient under the same test condition than that of three blades Savonius wind turbine Fig.2.

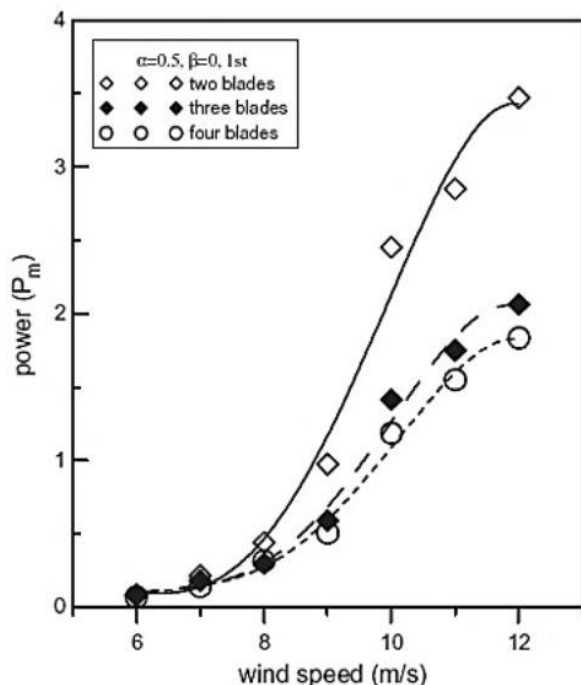


Figure 1.6 Power output of savonius rotor with respect to number of blades

ii. Effect of Aspect Ratio

The aerodynamic performance of the Savonius rotor depends strongly on the aspect ratio (AR). Tested different configurations for aspect ratios (noted α) of 0.5, 1, 2, 4, 5 by keeping other parameters constant, the results show that the power coefficient increases with the rise in aspect ratio Fig.2., Lately, studies with various designs of changed Savonius rotor having low ARs have been reported out. According to studies The rotor with an aspect ratio of 0.7 is having a maximum C_p equal to 0.21. Concluded that an AR of 0.77 leads to a maximum C_p of 0.24 However, several studies on Savonius new rotors use AR near to 1, generally the use of ARs within the range of 1.5–2.0 set good results on the performance of the Savonius rotor.

iii. Effect of Overlap Ratio

The overlap ratio is a major parameter that influences the structure of the flow inside the rotor and consequently its aerodynamic performances, the influence of the overlap ratio has been widely investigated, however there is not an accord among the outcomes acquired in previous studies. According to some studies the optimal value of overlap ratio is in the range of 0.1 to 0.15. It is indicated that the primary overlap ratio must be between 0.15 and 0.3 and the optimal value equal to 0.242. Also investigation on the effect of overlap ratio indicates that the configuration of Savonius rotor that shows the best performance is the one where the overlap ratio equal to 0.15, which gives an averaged power coefficient equal to 0.3161 for the TSR of 1.25.

Chapter 2

Mathematical Model

2.1 Introduction

The governing equations of fluid dynamics, which comprise mass continuity, momentum, energy, species transport, and turbulence closure equations, are the foundation of CFD. These equations are mathematical expressions of the fundamental physical concepts that underpin fluid dynamics: mass conservation, Newton's second law, energy conservation, and so on (Anderson, 2009). The governing equations that underpin the CFD software used in this thesis are initially presented in this chapter. The ANSYS is then given a brief introduction. This chapter also includes a mathematical examination of fluid loads on horizontal- and vertical-axis turbines, as well as an explanation of the theory behind the ANSYS model.

2.2 Governing Equations

The basic equations of fluid motion are derived by applying physical concepts of mass, momentum, and energy conservation to an appropriate flow control volume (see e.g. Anderson, 2009). The governing continuity and momentum equations, as well as accompanying boundary conditions, are presented in this section, which serve as the foundation for the CFD models utilized in the thesis. The fluid is assumed to be incompressible in this case.

2.2.1 Continuity Equation

The mass continuity equation is derived from the law of mass conservation. Consider a very small control volume (White, 2010). The time-rate-of-change of mass of the fluid element is zero as its elemental control volume moves with the flow (Anderson, 2009). The principle of conservation of mass can be stated in a Eulerian form for an arbitrary volume V . Invoking the physical meaning of the substantial derivative, we have

$$\frac{d}{dt} \int \rho dV = 0 \quad (2.1)$$

Where t is time, ρ is fluid density, and V is control volume.

Using the Reynolds transport theorem for the flux of mass through the volume surface A , Equation (2.1) can be rewritten as follows (Viola, 2018):

$$\frac{d}{dt} \int \rho dV = \int \frac{\partial}{\partial t} \rho dV + \int \rho \vec{u} * \vec{n} dA = 0 \quad (2.2)$$

Where \vec{n} is the normal vector to the surface A and \vec{u} is the flow velocity vector.

Using the Gauss divergence theorem, this becomes

$$\int \frac{\partial \rho}{\partial t} dV + \int \rho \vec{u} * \vec{n} dA = \int \left(\frac{\partial \rho}{\partial t} + \nabla * p \vec{u} \right) dV = 0 \quad (2.3)$$

For any arbitrary control volume, the argument is identically zero, such that

$$\left(\frac{\partial \rho}{\partial t} + \nabla * p \vec{u} \right) = 0 \quad (2.4)$$

2.2.2 Momentum Equation

The conservation of momentum equation is obtained from application of Newton's second law of motion ($\vec{F} = m\vec{a}$, where \vec{F} is force vector, m is the mass of the fluid, and \vec{a} is the fluid acceleration vector) to the fluid volume (Kundu et al., 2016). The change in momentum of a fluid volume is equal to the sum of the forces acting on the volume (Viola, 2018), such that

$$\frac{d}{dt} \int \rho \vec{u} dV = \vec{F} \quad (2.7)$$

Consider the moving fluid element (or an infinitely small volume $dV = dx_i x_j x_k = dx dy dz$) shown in Figure 2.1(a). The net force on the fluid element is equal to the product of its mass m and acceleration \vec{a} (Anderson, 2009). The force vector \vec{F} is comprised of body force and surface force vector components. The body force vector \vec{F}_{body} acts directly on the volumetric mass of the fluid element (e.g. gravity). The surface force vector \vec{F}_{surf} acts on the surface of the fluid element, incorporating the effects of pressure, shear, and normal stress distributions on the surface (Anderson, 2009):

$$\vec{F} = \vec{F}_{body} + \vec{F}_{surf} \quad (2.8)$$

The surface force vector \vec{F}_{surf} is due to the stresses on the sides of control surface. The stress vector relation is defined with three Cartesian components, acting on each face of the volume (see Figure 2.1(b)).

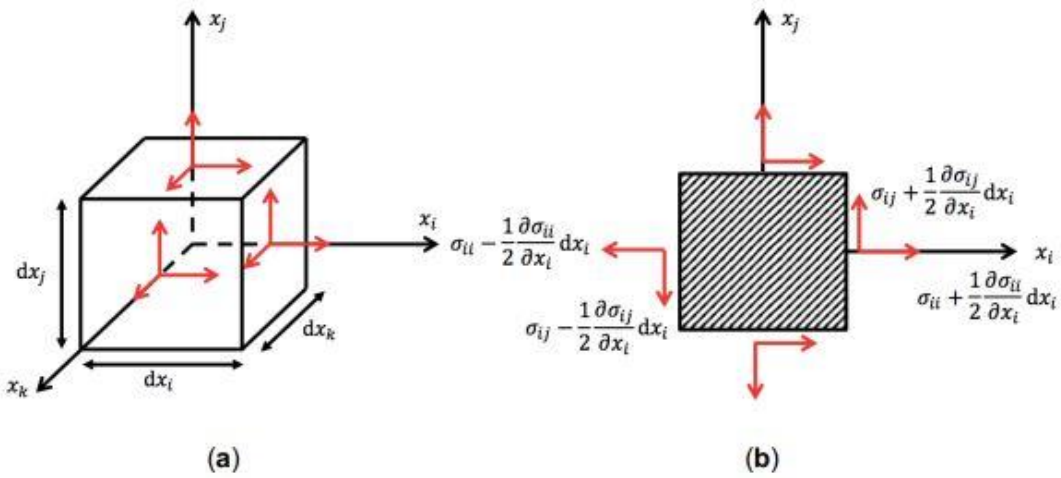


Figure 2.1 (a) Infinitesimally small, moving control volume dV ; and (b) notation for stresses in the xy plane (Viola, 2018).

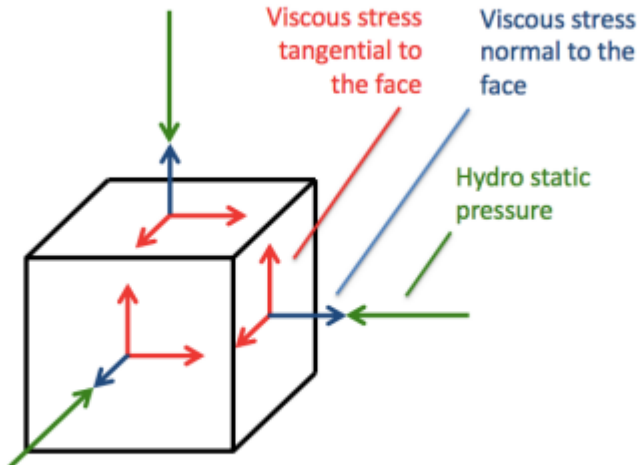


Figure 2.2. Shear stress tensor and pressure (Viola, 2018).

The stress components σ_{ij} are defined at the centre of the volume, as sketched in Figure 2.1(b) for the $x-y$ plane, using two subscripts: the first subscript i refers to the face on which the stress acts; the second subscript j refers to the direction of the stress. In short, σ_{ij} is the stress component in the j direction on a face normal to the i axis. The stress components σ_{ij} are divided into those due to the hydrostatic pressure p and those due to viscous effects τ_{ij} , indicated in

Figure 2.2. The hydrostatic pressure p is defined positive in compression, while the stresses σ_{ij} are defined positive in traction.

The surface forces are therefore the sum of p and τ_{ij} that arise from the motion of fluid with velocity gradients:

$$\sigma_{ij} = \begin{vmatrix} -p + \tau_{xx} & \tau_{yx} & \tau_{zx} \\ \tau_{xy} & -p + \tau_{yy} & \tau_{zy} \\ \tau_{xz} & \tau_{yz} & -p + \tau_{zz} \end{vmatrix} \quad (2.10)$$

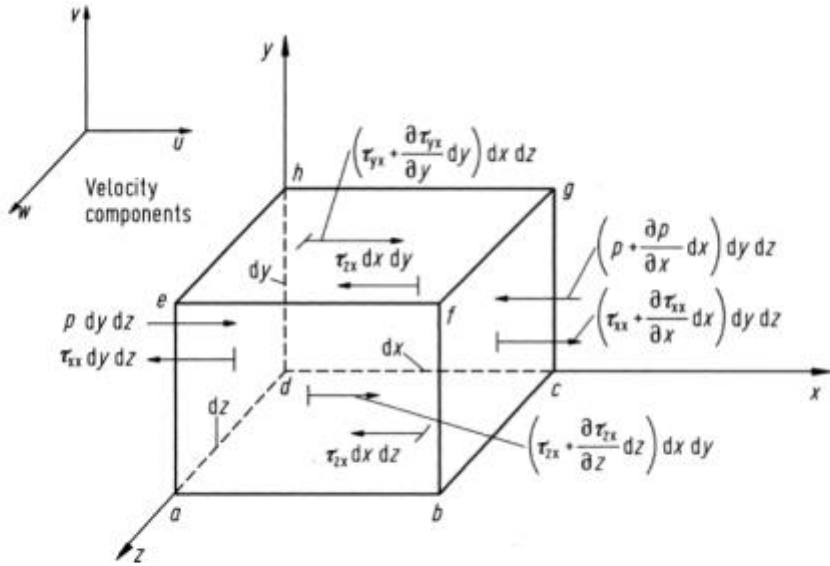


Figure 2.3. Elemental Cartesian fixed control volume showing surface force components in the x -direction only (Anderson, 2009).

The shear and normal stresses in a fluid are related to the time-rate-of-change of the deformation of the fluid element. The shear stress (such as τ_{xy} in Figure 2.3) is related to the time rate-of-change of the shearing deformation of the fluid element, whereas the normal stress (for example τ_{xx} in Figure 2.3) is related to the time-rate-of-change of volume of the fluid element. As a result, both shear and normal stresses depend on velocity gradients in the flow. In most viscous flows, normal stresses are much smaller than shear stresses, and can be neglected. When the normal velocity gradients (e.g. denoted by $\frac{\partial u}{\partial x}$) are very large, normal stresses then become significant, such as inside a shock wave (Anderson, 2009). The net surface force in the x direction $\vec{F}_{x,surf}$ for the moving fluid element thus can be written:

$$d\vec{F}_{x,surf} = \left[\frac{\partial}{\partial x}(\sigma_{xx}) + \frac{\partial}{\partial y}(\sigma_{yx}) + \frac{\partial}{\partial z}(\sigma_{zx}) \right] dx dy dz$$

It may be seen that this force is proportional to the element volume. The net surface force is split into pressure and viscous stresses terms. We obtain the x, y and z force components per unit volume $dV = dx dy dz$ on the control surface as (White, 2010):

$$d \frac{\vec{F}_{x,surf}}{dV} = -\frac{\partial p}{\partial x} + \frac{\partial}{\partial x}(\tau_{xx}) + \frac{\partial}{\partial y}(\tau_{yx}) + \frac{\partial}{\partial z}(\tau_{zx}) \quad (2.12)$$

$$d \frac{\vec{F}_{y,surf}}{dV} = -\frac{\partial p}{\partial y} + \frac{\partial}{\partial x}(\tau_{xy}) + \frac{\partial}{\partial y}(\tau_{yy}) + \frac{\partial}{\partial z}(\tau_{zy}) \quad (2.13)$$

$$d \frac{\vec{F}_{z,surf}}{dV} = -\frac{\partial p}{\partial z} + \frac{\partial}{\partial x}(\tau_{xz}) + \frac{\partial}{\partial y}(\tau_{yz}) + \frac{\partial}{\partial z}(\tau_{zz}) \quad (2.14)$$

The net vector surface force is thus expressed as: Denklemi buraya yazın.

$$(\frac{d\vec{F}}{dV})_{surf} = -\nabla p + (\frac{d\vec{F}}{dV})_{viscous} \quad (2.15)$$

Or

$$(\frac{d\vec{F}}{dV})_{viscous} = \nabla * \tau_{ij} \quad (2.16)$$

The surface force is thus the sum of the pressure gradient vector and the divergence of the viscous stress tensor. Substituting into Eq. (2.7) and utilizing Eq. (2.8), the basic differential momentum equation for an infinitesimal element is derived as (White, 2010)

$$\rho \frac{D\vec{u}}{Dt} = \rho \vec{f} - \nabla p + \nabla * \vec{\tau}_{ij} \quad (2.17)$$

where $\vec{u} = (u, v, w)$ and

$$\frac{D\vec{u}}{Dt} = \frac{\partial \vec{u}}{\partial t} + u \frac{\partial \vec{u}}{\partial x} + v \frac{\partial \vec{u}}{\partial y} + w \frac{\partial \vec{u}}{\partial z} \quad (2.18)$$

The terms in Eq. (2.17) have the following physical meaning:

density X acceleration

= *body force per unit volume + pressure force per unit volume + viscous force per unit volume.*

$$\begin{aligned} \tau_{xx} &= \lambda \nabla \cdot \vec{u} + 2\mu \frac{\partial u}{\partial x}, & \tau_{yy} &= \lambda \nabla \cdot \vec{u} + 2\mu \frac{\partial v}{\partial y}, & \tau_{zz} &= \lambda \nabla \cdot \vec{u} + 2\mu \frac{\partial w}{\partial z}, \\ \tau_{xy} &= \tau_{yx} = \mu \left(\frac{\partial u}{\partial y} + \frac{\partial v}{\partial x} \right), & \tau_{xz} &= \tau_{zx} = \mu \left(\frac{\partial w}{\partial x} + \frac{\partial u}{\partial z} \right), \\ \tau_{yz} &= \tau_{zy} = \mu \left(\frac{\partial v}{\partial z} + \frac{\partial w}{\partial y} \right), \end{aligned} \quad (2.19)$$

Where μ is the molecular viscosity coefficient and λ is the bulk viscosity coefficient. Stokes made the hypothesis that

$$\lambda = -\frac{2}{3}\mu \quad (2.20)$$

By including Eq. (2.18) and Stoke's hypothesis in the momentum equation, the following Navier-Stokes momentum equation (in tensor form) is obtained:

$$\rho \frac{u_i}{dt} = \rho f_i - \frac{\partial p}{\partial x_i} + \mu \frac{\partial^2 p}{\partial x_i \partial x_j} + (\mu + \lambda) \frac{\partial}{\partial x_i} \left(\frac{\partial u_j}{\partial x_j} \right) \quad (2.21)$$

For an incompressible fluid, $\nabla * \vec{u} = \frac{\partial u_j}{\partial x_j} = 0$, and the Navier-Stokes momentum equation reduces to the following equation:

$$\rho \frac{d\vec{u}}{dt} = \vec{F} - \nabla p + \mu \nabla^2 \vec{u} \quad (2.22)$$

Dividing through by the fluid density, the Navier-Stokes momentum equation for an incompressible Newtonian fluid may be written:

$$\frac{D\vec{u}}{Dt} = -\frac{1}{\rho} \nabla p + \nu \nabla^2 \vec{u} + \frac{1}{\rho} \vec{F} \quad (2.23)$$

in which \vec{u} is the velocity field vector, ρ is fluid density, p is pressure, ν is fluid kinematic viscosity, and \vec{F} is the body force vector exerted on the fluid. In the present work, \vec{F} is the sum of the gravitational force and the force exerted by the turbines. In tensor notation, after Reynolds-averaging, Eq. (2.23) may be written

$$\frac{D\bar{u}_i}{Dt} = -\frac{1}{\rho} \frac{\partial p}{\partial x_i} + \frac{\partial}{\partial x_j} \left[(\nu + v_t) \left(\frac{\partial \bar{u}_i}{\partial x_j} + \frac{\partial \bar{u}_j}{\partial x_i} \right) \right] + F_i, \quad (2.24)$$

where \bar{u}_i is the i -th Reynolds-averaged velocity component ($i = 1, 2, 3$, corresponding to the x, y, z directions), v_t is the turbulence viscosity coefficient due to subgrid-scale turbulence, and F_i is the i -th force component divided by mean flow density ρ per unit volume (Creech et al., 2015).

2.2.3 Energy Equation

The first rule of thermodynamics states that the rate of energy change inside the control volume equals the total of the net flow of heat into the volume and the rate of work done on the volume owing to body and surface forces when applied to an infinitesimal moving fluid element as shown in Figure 2.3. (Anderson, 2009)

The customary form of the general differential energy equation is

$$\rho \frac{de}{dt} + p(\nabla * \vec{u}) = \nabla * (k\nabla T) + \varphi \quad (2.25)$$

where e is the internal energy per unit mass of the fluid element, k is the thermal conductivity (a fluid property that varies with temperature T and pressure p in much the same way as viscosity), and φ is a viscous-dissipation function. The total energy of a moving fluid per unit mass is the sum of its internal energy per unit mass e , and its kinetic energy per unit mass $\frac{|\vec{u}|^2}{2}$. Hence, the total energy is $(e + \frac{|\vec{u}|^2}{2})$, noting that $|\vec{u}|^2 = u^2 + v^2 + w^2$ (White, 2010).

2.2.4 Boundary Conditions

The governing equations for the mass, momentum, and energy conservation laws require boundary and initial conditions in order to fully specify any fluid dynamics problem of interest.

Boundary conditions are applied at the edge of the solution space, and are usually defined prior to any simulation or model being run (Creech, 2009). Two main categories of boundary condition are considered:

At solid impermeable walls, the density and pressure are estimated by extrapolation of interior values. The internal energy is prescribed as a Dirichlet condition. The fluid velocity vector is prescribed so that its components are the same as the wall velocity components (i.e. no-slip condition). The fluid temperature is prescribed to be the same as that of the wall so that there is no temperature jump in a viscous heating-conducting fluid. In other words,

$$\vec{u}_{fluid} = \vec{u}_{wall}, \quad \vec{T}_{fluid} = \vec{T}_{wall} \quad (2.26)$$

At the flow inlet and outlet sections, the distribution of velocity \vec{u} , pressure p , and temperature T are given by transmissive Neumann conditions whereby the corresponding solution derivatives are applied. In practice, open boundaries can be prescribed in a number of ways, for instance using Dirichlet boundary conditions (with fixed flux values), Neumann boundary

conditions (where the velocity gradient is a constant), or even the combination of both of them (also called mixed or Robin conditions):

$$au + b \frac{\partial u}{\partial n} = g \quad (2.31)$$

for some non-zero constants a, b , a given function g , and normal derivative $\frac{\partial u}{\partial n}$ at the boundary (Creech, 2009).

At a liquid-gas interface or free surface, the conditions become more complicated, with the free surface elevation $\eta(x, y, t)$ matched to kinematic and dynamic boundary conditions

. In computational fluid dynamics (CFD), proper numerical implementation of the boundary conditions should give results that match the physical boundary conditions. This remains an important subject of current research in CFD (Anderson, 2009). The Dirichlet and the Neumann conditions presented above are two of the most widely used types of boundary conditions for finite volume solver. In mathematical terms, these conditions are respectively a value specified (or a first type) and a flux specified (or a second type) boundary condition (Moukalled et al., 2016)

Chapter 3

Car Aerodynamics

The origins of aerodynamics can be traced back to plane aerodynamics. However, there is a significant difference between planes and automobiles. Planes without aerodynamics cannot fly (their ability to fly is linked to their aerodynamics), yet vehicles with poor aerodynamics can still be driven. This concept is based on the fact that poor aerodynamics necessitates the use of greater power to move the vehicle; in the case of a plane, poor aerodynamics prevent it from flying. The primary goal of both aerodynamics and physics is to reduce drag (air resistance).

3.1 History

First of all, we should consider that the aerodynamics of the roof box and cars are very similar. Therefore, we are going to analyse the history and evolution of the aerodynamic of cars. The start of aerodynamic come from the aerodynamics of planes. However the difference between planes and cars is very different. Planes without aerodynamic cannot exist (their ability to fly is due to their aerodynamic), but in cars it is possible to road without a good aerodynamic design. This idea is due to a bad aerodynamic affects to the need of a more power to move the vehicle, in a plane a bad aerodynamic does not allow to fly. The primordial objective of both aerodynamics is to reduce drag (air resistance).

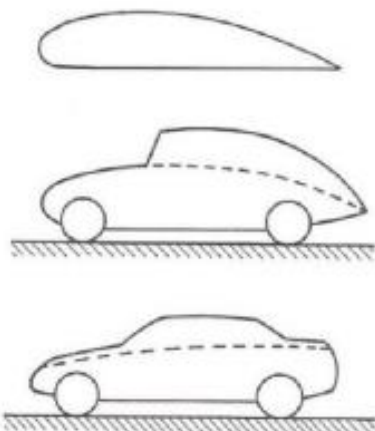


Figure 3.1 Comparison of a plane wing profile and evolution of cars.

The main differences of planes and cars aerodynamics are the following:

- Cars work really near from the ground compared with their dimensions. Therefore, the ground effect cannot be ignored.
- In the point of view of cars aerodynamics, cars should be considered as one element. They cannot be separated in components. Planes can be analysed component to component.
- Car aerodynamic has an important experimental development, above all the

This is the start of cars, and the first impressions were copying the forms of planes and ships. The first engineers ignored the ground effect and the loss of symmetry of the flow. Therefore, this ignorance in these effects makes an increase of drag. They also ignored that wheels being out of the chassis of the car makes the flow distorted [11]. Consequently, the air resistance increase and all the improvements done in the chassis of the car cannot be denoted in the total of the vehicle.



Figure 3.2 First prototypes of cars based in planes and ships forms (Jamais Contente and Alfa Romeo of 1914)

In this period appeared the first wind tunnel to improve the aerodynamic of vehicles. The aim of the first wind tunnels were not determinate the aerodynamic forces; the objective was determinate the forms of the vehicles to reduce the power needed to move the car in certain values of speed.

We have to remark Paul Jaray's work, who was the first engineer designing a car keeping in mind the aerodynamics. His designs were based in planes and really aerodynamics. However, his design were not accepted by consumers. After some years of his creations, other engineers started to use his ideas in their designs.

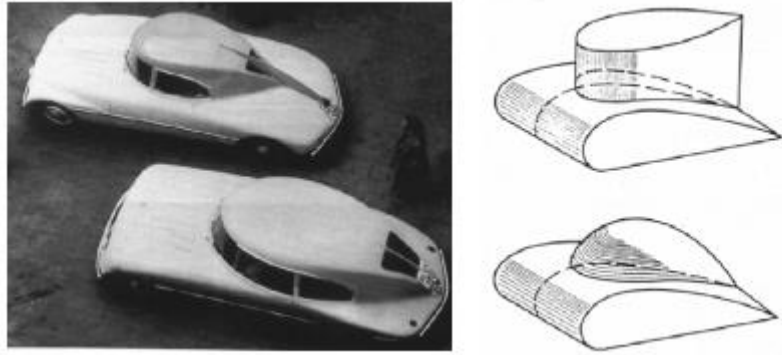


Figure 3.3 Jaray's Design

In this period started to obtain special importance the aerodynamic of the cars. The objective is reduce the drag resistance to reduce the fuel consumption. There are two ways to reduce the drag resistance:

- Reducing frontal area. This consist to reduce the area which the air impact. In this way, the reduction of area reduces the drag resistance.
- Improving the aerodynamics of the car to reduce CD. Nowadays, the first option is not possible. All the manufactures have arrived at the same equation of optimization.

$$A = 0.81 \cdot (b \cdot h)$$

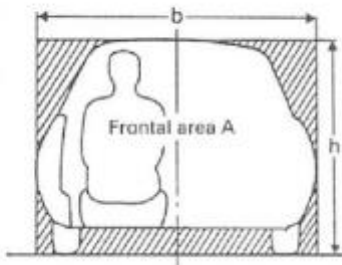


Figure 3.4 A is frontal area; b is wide; h is height

In seventies, due to the fuel crisis, engineers started to improve the details and optimize the global aerodynamic of the vehicle. As the result they had decreased the drag coefficient to values of 0.3.

Nowadays with efficiency as the main word in people mind, it is impossible the creation of a new car without thinking in the aerodynamics. For example, in 2013 appears the most aerodynamic production car. This car is Mercedes-Benz CLA which CD is 0.23 [19]. This value

was obtained with the improvement and optimization of details like engine cover, optimized front, mirrors and other elements



Figure 3.5 Mercerdes-Benz CLA which CD is 0.23

3.2 Flow Around a Car

Figure 3.1 shows how a vehicle traveling on a road encounters several types of resistance. The sum of rolling resistance, gravity resistance, acceleration resistance, and aerodynamic drag resistance on a moving vehicle with constant velocity is the total resistance force. To propel the vehicle ahead, these opposing forces must be overcome. The equation of motion is used to express the total resistance, Eq (3.1).

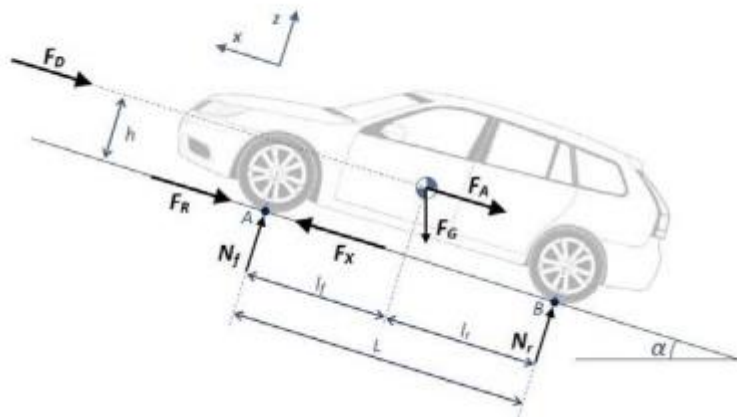


Figure 3.1 Resistances on a car

$$F_x = F_A + F_R + F_G + F_D = ma + fmg\cos\alpha + mgsin\alpha + \frac{1}{2}\rho C_D A_f U^2 \quad (3.1)$$

The inclination resistance is independent of the velocity and since CFD calculations are performed on flat road, the inclination resistance can be neglected. During the lower velocities,

the rolling resistance is the dominating resistance force. For velocities above 90km/h the aerodynamic drag will be the dominating resistance due to the fact that the drag is increasing with the square of the speed. Figure 3.2 shows the rolling resistance and the aerodynamic resistance as a function of the velocity, the rolling resistance slightly increase with the total resistance but can be assumed constant for velocities below 100 km/h.

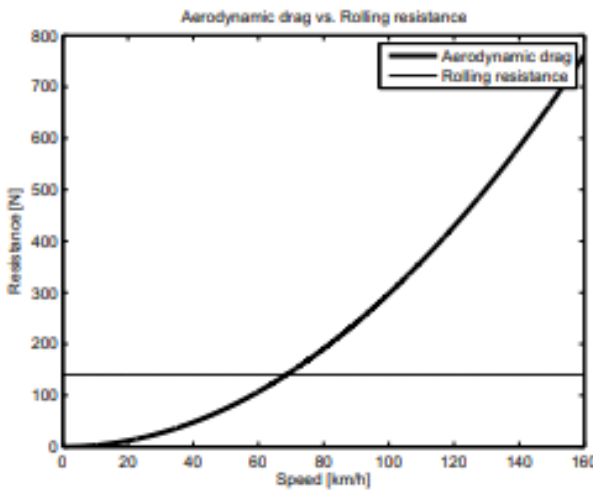


Figure 3.2 Aerodynamic drag and rolling resistance versus velocity

The aerodynamic drag force can be divided into two components, form and friction force. The form (pressure) drag acts in the direction normal to the surfaces, meanwhile the friction force is acting tangential to the surface. Due to the scale and shape of a passenger car the form drag is dominating and the vehicle can be assumed to be a bluff body. This means that a big wake and vortices will be present in the flow field. The form drag is created by the pressure difference between the front and rear part of the vehicle. The friction on the surface is a source of energy loss since the air flow slows down near the surface and will eventually separate from the body. Since the pressure distribution over the body is not symmetric and the pressure on the rear will be lower than in the front, there will be rearward directed drag force. Due to Bernoulli's equation, Eq (3.2), it can be seen that the high pressure peak in the front indicates that the velocity will be low at that point, stagnation point. Further downstream, the pressure is decreased at the same time as the velocity rises, this corresponds to the Bernoulli's equation.

$$p_1 + \frac{\rho V_1^2}{2} = p_2 + \frac{\rho V_2^2}{2} \quad (3.2)$$

The friction force is created due to shear stressed between the fluid and the surface of the body and will be the sum of all the shear forces in the fluid. The greatest contribution of the friction drag comes from the areas with attached flow.

3.2.1 Drag and Lift

The drag coefficient is a dimensionless quantity that describes a vehicles aerodynamic resistance and is a useful tool when comparing different vehicle shapes regardless of size and speed. The drag coefficient can be expressed as Eq. 3.3. The drag coefficient can be divided into two components, a friction and a form components, as described section 3.1.

$$C_d = \frac{F_D}{\frac{1}{2}\rho U^2 A} \quad (3.3)$$

where ρ = air density, U = freestream velocity, F_D = drag force and

A = frontal area

When air streams around a body, there will be a pressure difference between the upper and lower part, if no separation occurs in the flow field, the air on the upper surface will travel a longer path to reach the end of the vehicle. This difference in travel length will create a difference in the speed of the fluid flow, longer way to travel will give a higher speed, and lower pressure. On a vehicle the pressure will be lower on top of the vehicle and higher underneath it, this gives the lifting force. The lift coefficient is a dimensionless coefficient that describes the lift generated on the body and is expressed as:

$$C_L = \frac{F_L}{\frac{1}{2}\rho U^2 A} \quad (3.3)$$

3.3 Drag coefficient

This coefficient is a dimensionless value that allows to quantify the drag resistance of an object. When this value is low indicates that the object has less aerodynamic drag. The drag coefficient depends with the shape and position of the object (projected area) and the properties of fluid (kind of fluid, density, speed...).

In the following images there are some examples of the C_D depending on the shape or vehicle shapes. As we see the area of impact and the shapes of impact are very important to reduce the

value of drag coefficient.

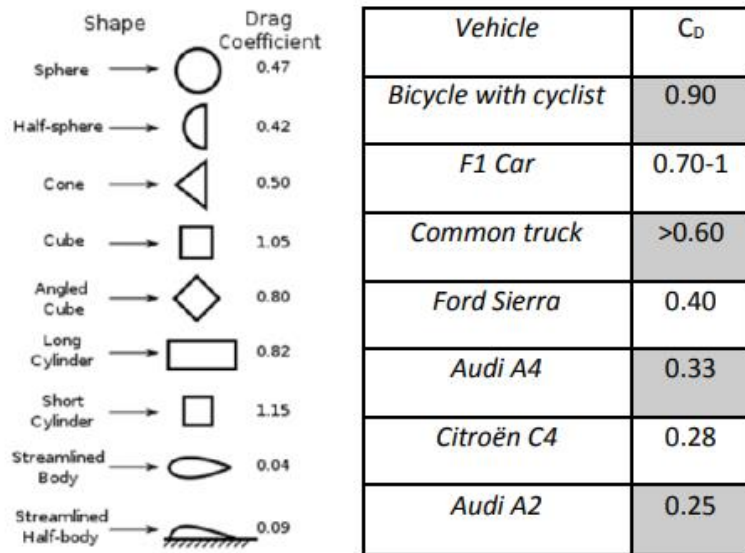


Figure 3.3 C_D of different shapes and cars

3.4 Ground Effect

The ground effect is called to the aerodynamic action when a body has a differential pressure between the top and the bottom of the car. The pressure that appears on the top of the car is higher than the pressure of the ground vehicle, therefore this differential makes car to smash the ground. This effect helps to increase the grip and it allows the car to increase its velocity in corners.

This effect is very common in competition cars. Due to the ground effect car can go faster in the turns without losing grip.



Figure 3.4 Lotus F1 Car

Chapter 4

Geometry Selections and ANSYS Analysis

This chapter is to select geometries. The turbine types will be compared and the best fit will be used in car. Further, geometry for car will be selected and some designs of air ducts will be analyzed.

4.1 Vehicle Selection

This idea is an innovative, so that an innovative car is selected for analyzing. Tesla CyberTruck is chosen to analyze. From previous studies, it is obtained that it has drag coefficient of 0.48.



Figure 4.1 Tesla Cyber Truck

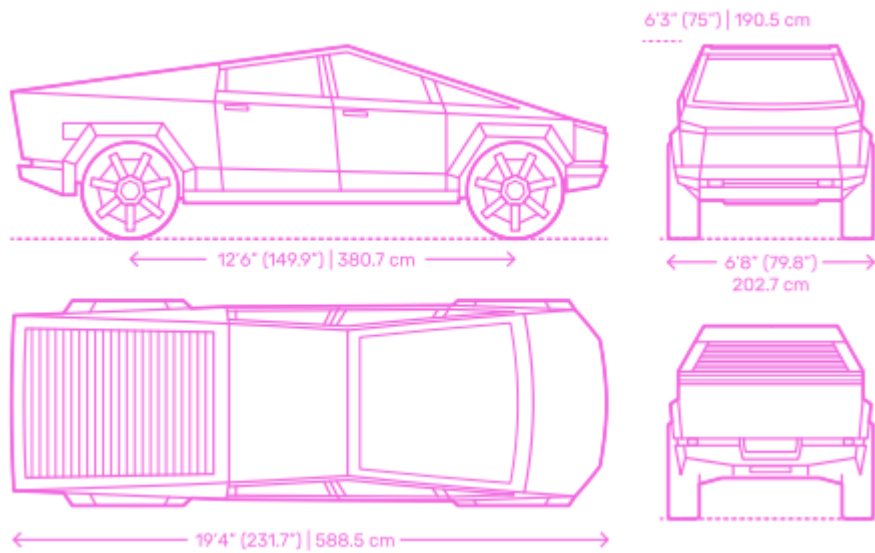


Figure 4.2 Dimension of Cyber Truck

4.1.1 SolidWorks Drawing of Selected Vehicle

In this paper, SolidWorks 2019 is used to draw solid geometries. An image of CyberTruck is used to sketch on.

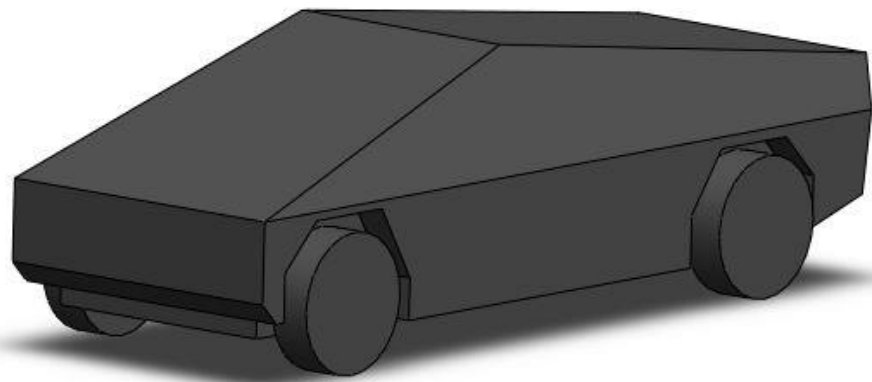


Figure 4.3 Cybertruck drawn in SolidWorks

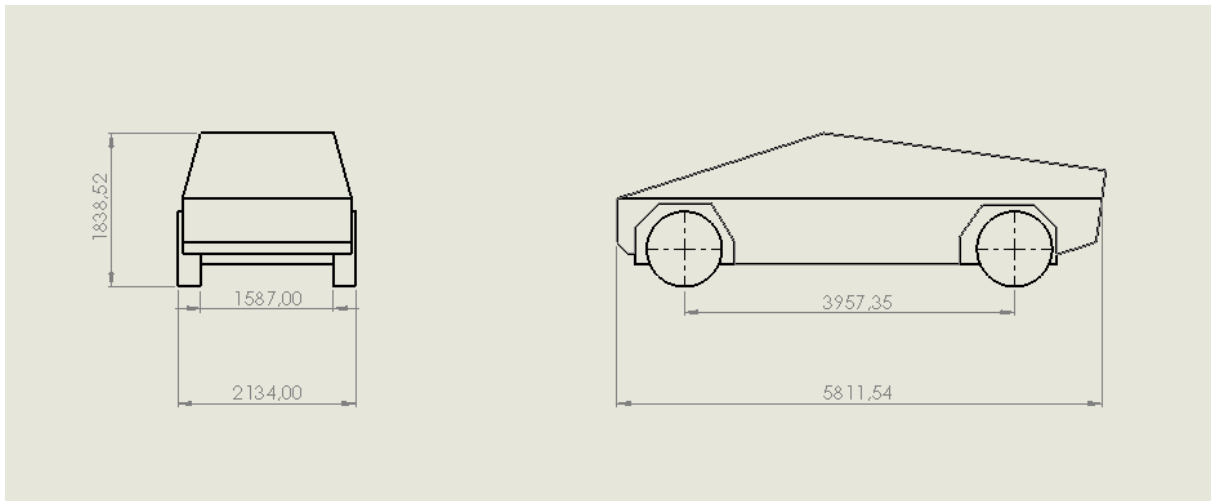


Figure 4.4 Technical Drawing of selected vehicle

The SolidWorks file turned to .step to use it in ANSYS. Meshing is done.

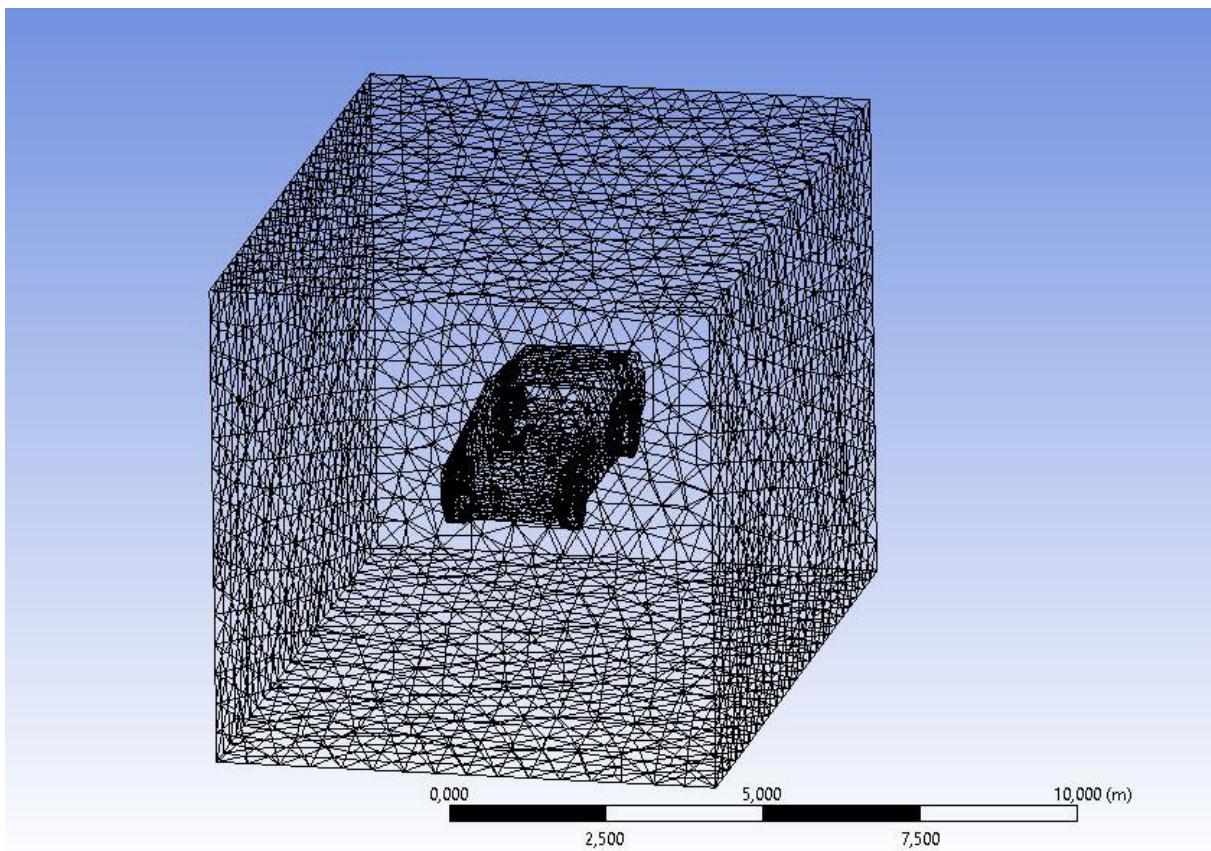


Figure 4.5 Mesh Structure of the vehicle

Mesh Quality

Name	Type	Min Orthogonal Quality	Max Aspect Ratio
solid	Tet Cell	0.22721408	13.288667

Orthogonal Quality

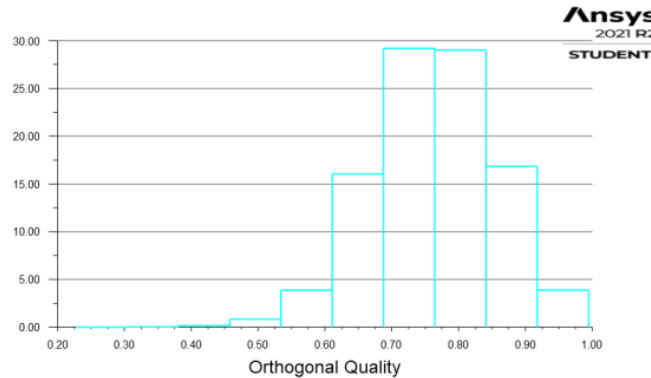


Figure 4.6 Mesh Properties of Simulation 1

Max Aspect Ratio is below 80 and average quality is 0.78. It is okay according to other studies.

— Inlet	
— inlet	
Velocity Specification Method	Magnitude, Normal to Boundary
Reference Frame	Absolute
Velocity Magnitude [m/s]	25
Supersonic/Initial Gauge Pressure [Pa]	0
Turbulent Specification Method	Intensity and Viscosity Ratio
Turbulent Intensity [%]	5
Turbulent Viscosity Ratio	10
— Outlet	
— outlet	
Backflow Reference Frame	Absolute
Gauge Pressure [Pa]	0
Pressure Profile Multiplier	1
Backflow Direction Specification Method	Normal to Boundary
Turbulent Specification Method	Intensity and Viscosity Ratio
Backflow Turbulent Intensity [%]	5
Backflow Turbulent Viscosity Ratio	10
Backflow Pressure Specification	Total Pressure
Build artificial walls to prevent reverse flow?	no
Radial Equilibrium Pressure Distribution	no
Average Pressure Specification?	no

Figure 4.7 Boundary conditions of Simulation 1

Inlet velocity is chosen as 90 km/hr. The same conditions will be applied for velocity of 10 km/hr to 90 km/hr.

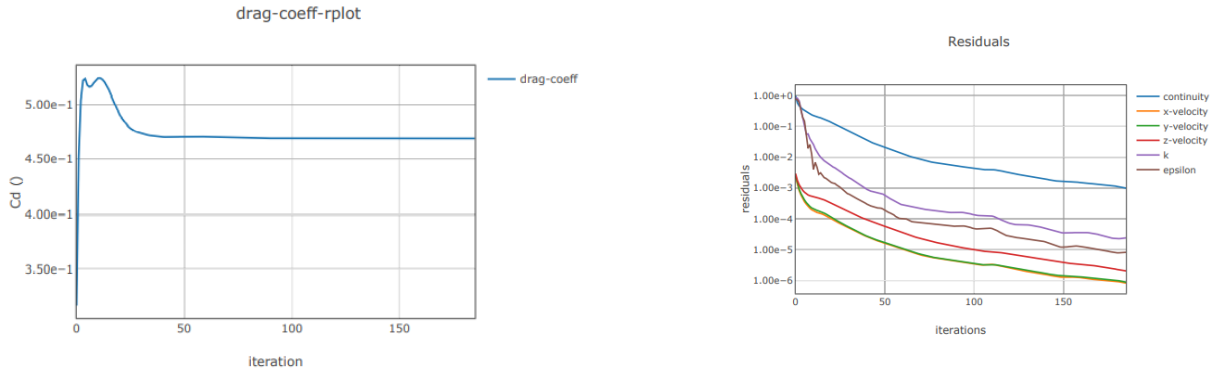


Figure 4.8 (a)Drag coefficient by iteration taken from ANSYS Report (b) Residuals

drag-coeff	0.4687926
drag-force	629.5809 N

Figure 4.9 Drag force and drag coefficinet calculated by ANSYS Software

Table 4.1 Residuals

	Value	Absolute Criteria	Convergence Status
continuity	0.0009959231	0.001	Converged
x-velocity	8.249143e-07	0.001	Converged
y-velocity	8.858748e-07	0.001	Converged
z-velocity	2.05405e-06	0.001	Converged
k	2.421631e-05	0.001	Converged
epsilon	8.251946e-06	0.001	Converged

It is seen that every residuals are okay for CFD simulation. Continuity residual is converged under 10e-03, Although it is not healthiest CFD result, it can be considered as OK.

4.2 Air Duct Design 1.

There will be 2 designs for air ducts. This is the first of them. There are 2 air ducts located in sides.

It is found that drag coefficient is 0.47. Previous studies claims it is 0.48. The simulation and drawing of the geometry is adequate to analyze.

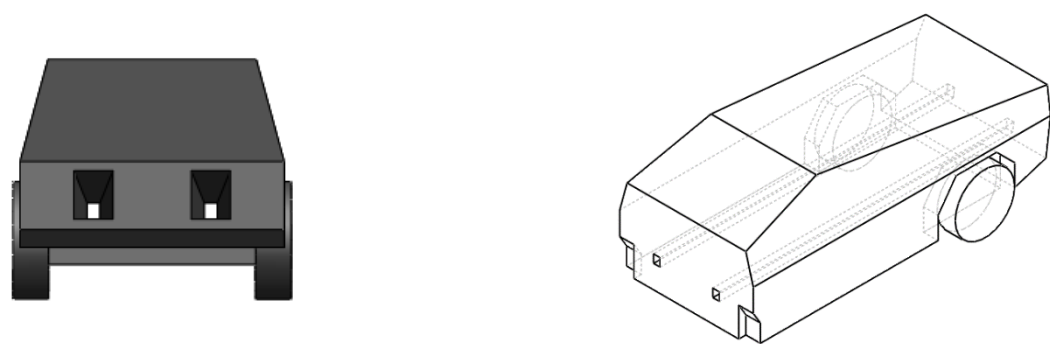


Figure 4.10 (a) Front view of Design 1 (b) Section view of Design 1

The airducts get smaller inside car as there is not enough space due to some other components of car.

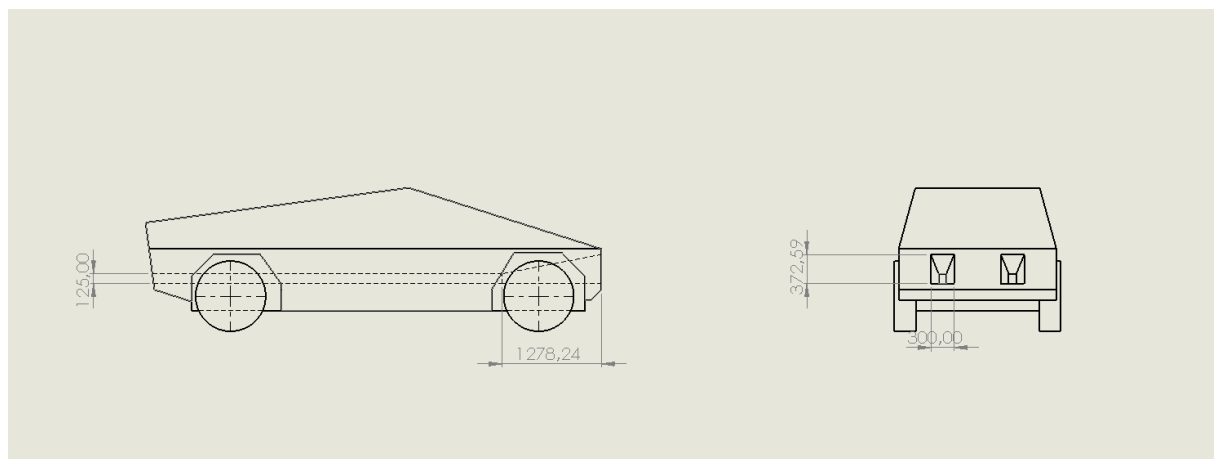


Figure 4.11 Technical Drawing of Design 1

The airducts has shape of 30 cm width to 372 cm heights, it gets smaller before it comes to passenger seat.

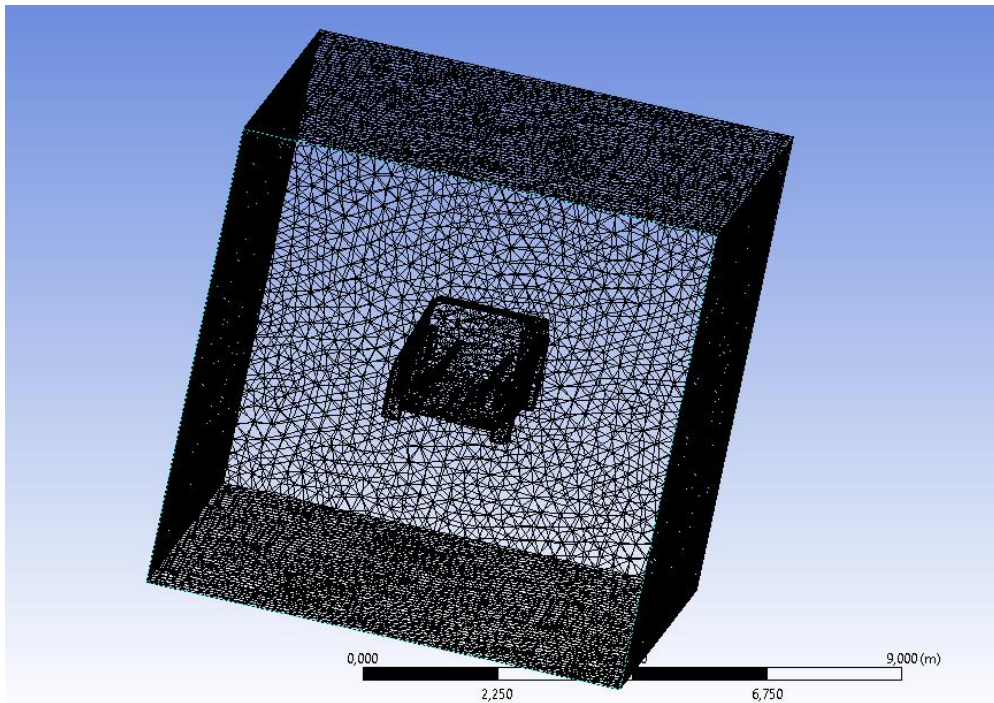


Figure 4.12 Meshig of Design 1

Mesh Quality

Name	Type	Min Orthogonal Quality	Max Aspect Ratio
solid	Tet Cell	0.23584919	13.512402

Orthogonal Quality

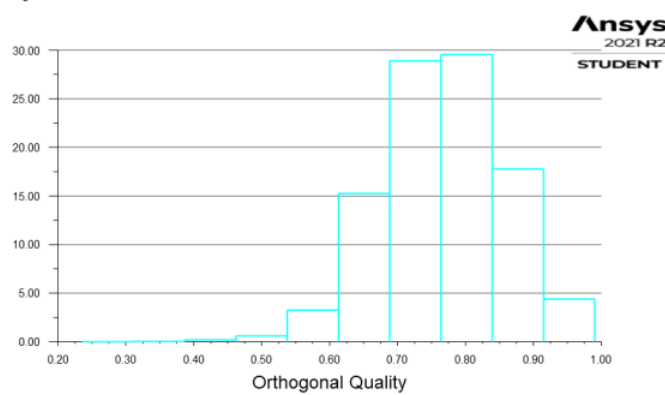


Figure 4.13 Mesh quality of design 1

Max Aspect Ratio is below 80 and average quality is 0.78. It is okay according to other studies.

— Inlet	
— inlet	
Velocity Specification Method	Magnitude, Normal to Boundary
Reference Frame	Absolute
Velocity Magnitude [m/s]	25
Supersonic/Initial Gauge Pressure [Pa]	0
Turbulent Specification Method	Intensity and Viscosity Ratio
Turbulent Intensity [%]	5
Turbulent Viscosity Ratio	10
— Outlet	
— outlet	
Backflow Reference Frame	Absolute
Gauge Pressure [Pa]	0
Pressure Profile Multiplier	1
Backflow Direction Specification Method	Normal to Boundary
Turbulent Specification Method	Intensity and Viscosity Ratio
Backflow Turbulent Intensity [%]	5
Backflow Turbulent Viscosity Ratio	10
Backflow Pressure Specification	Total Pressure
Build artificial walls to prevent reverse flow?	no
Radial Equilibrium Pressure Distribution	no
Average Pressure Specification?	no

Figure 4.14 Boundary conditions of Simulation 2

Inlet velocity is chosen as 90 km/hr. The same conditions will be applied for velocity of 10 km/hr to 90 km/hr.

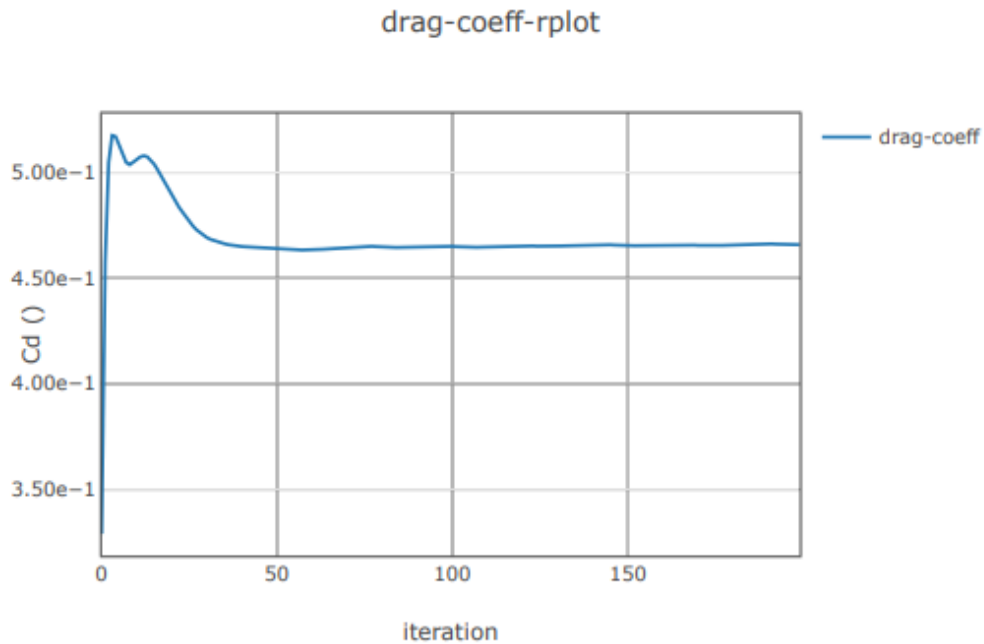


Figure 4.15 Drag coefficient by iteration taken from ANSYS Report

drag-coeff	0.4658079
drag-force	615.3707 N

Figure 4.16 Drag coefficient and force applied on vehicle design 1

Drag force and drag coefficient is decreased. The reduction in drag force is **14N**. It will be evaluated more in next sections.

4.3 Air Ducts Design 2

This is the first of them. There are 2 air ducts located in middle.

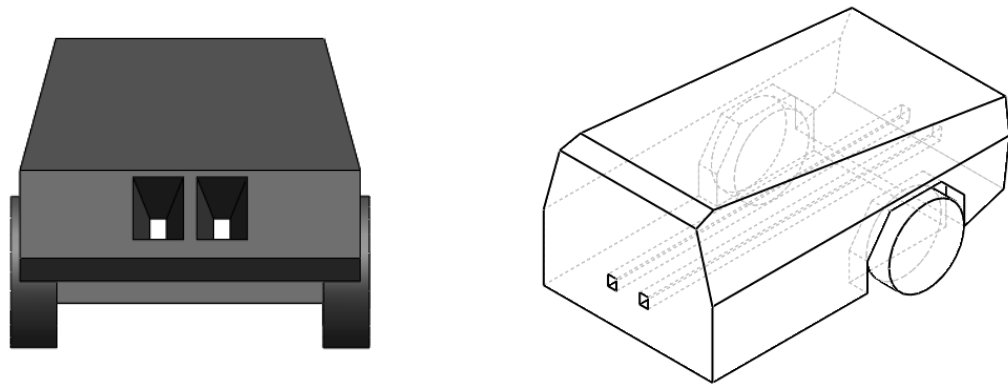


Figure 4.17 (a) Front view of Design 2 (b) Section view of Design 2

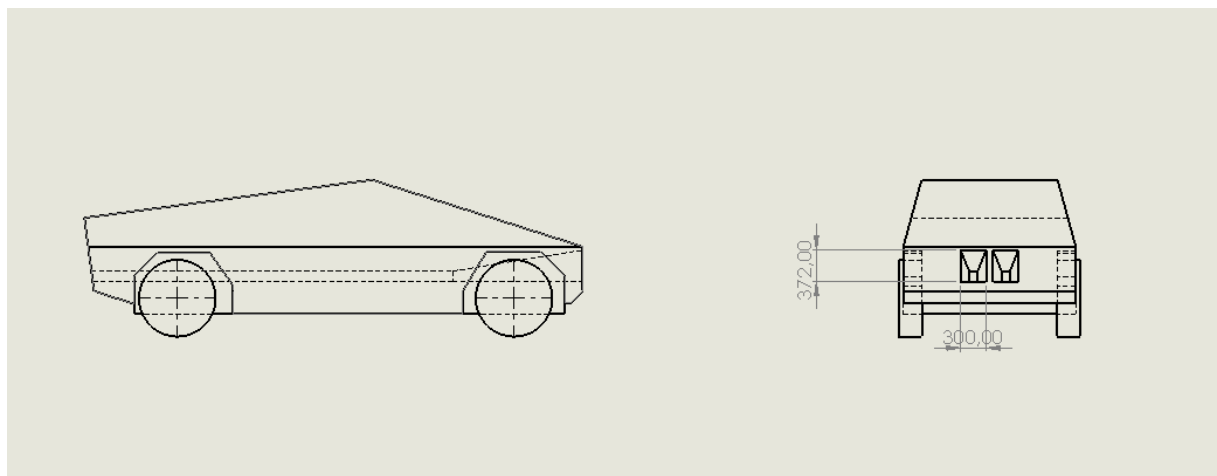


Figure 4.18 Technical Drawing of Design 2

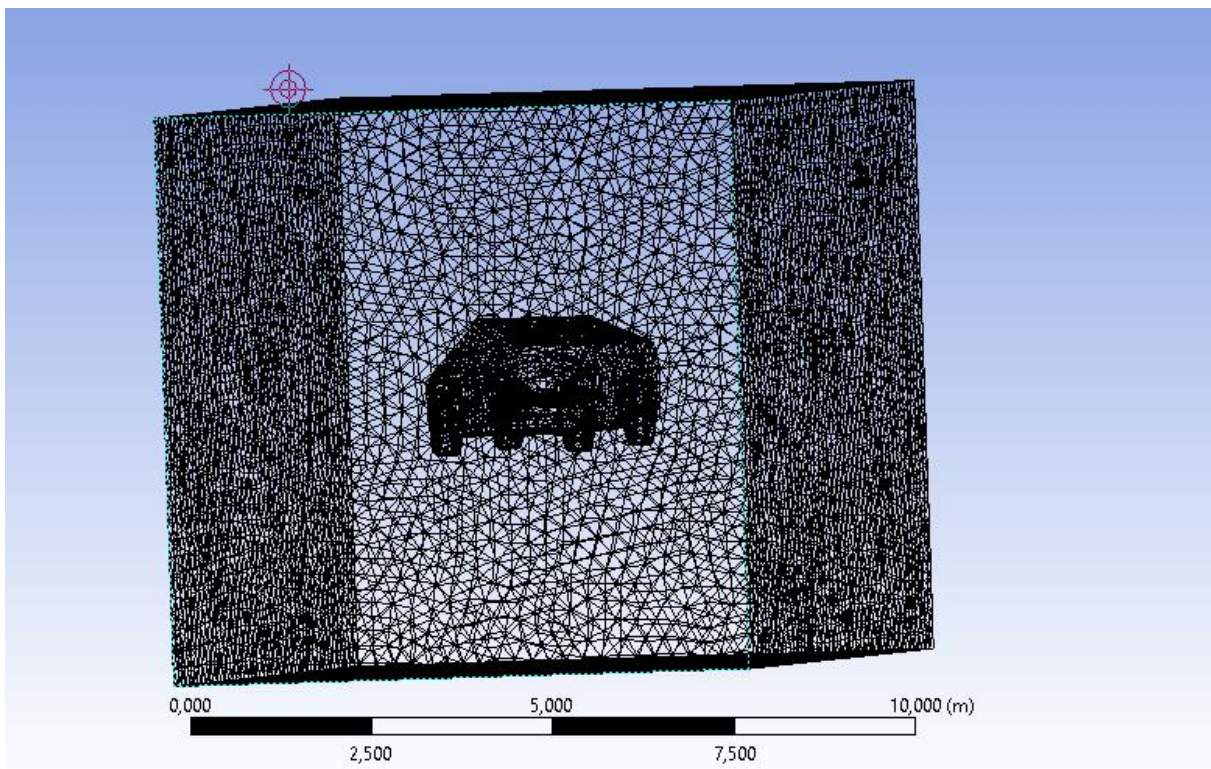


Figure 4.19 Meshing of Design 2

Mesh Quality

Cells	Faces	Nodes
187371	384679	36415

Name	Type	Min Orthogonal Quality	Max Aspect Ratio
solid	Tet Cell	0.075771444	35.097523

Orthogonal Quality

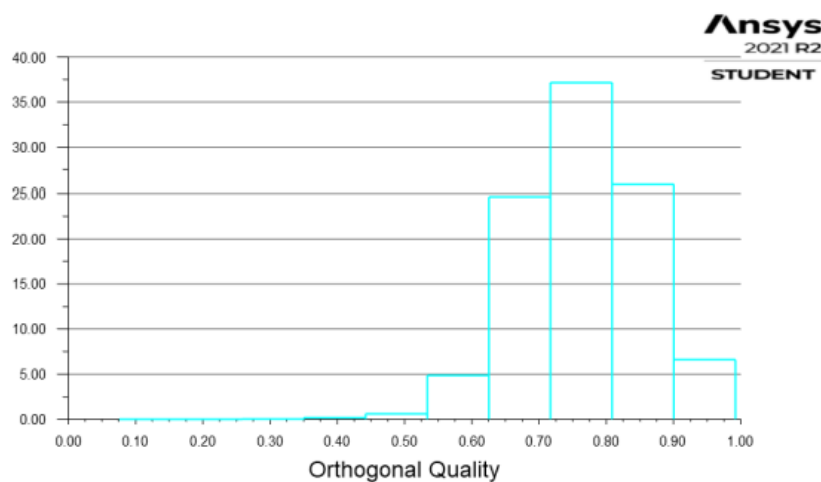


Figure 4.20 Mesh Quality of design 2

The inlet boundaries as same in other simulations.

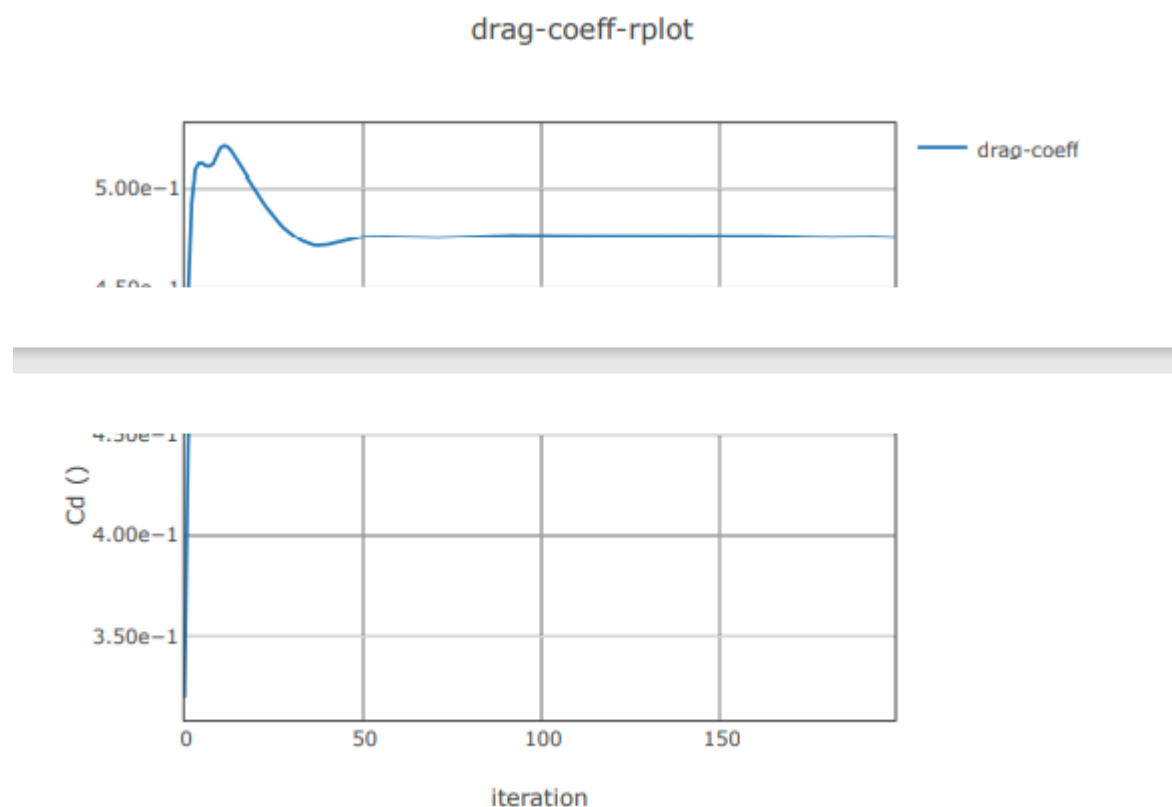


Figure 4.21 Drag coefficient by iteration taken from ANSYS Report

drag-force	629.2279 N
drag-coeff	0.4753928

Figure 4.22 Drag coefficient and force applied on vehicle design 2

4.4 Air Ducts Design 3

In this design, geometry of vehicle is changed. 300 milimeters plate is added in front panel of the automobile. This will help to set several turbines.

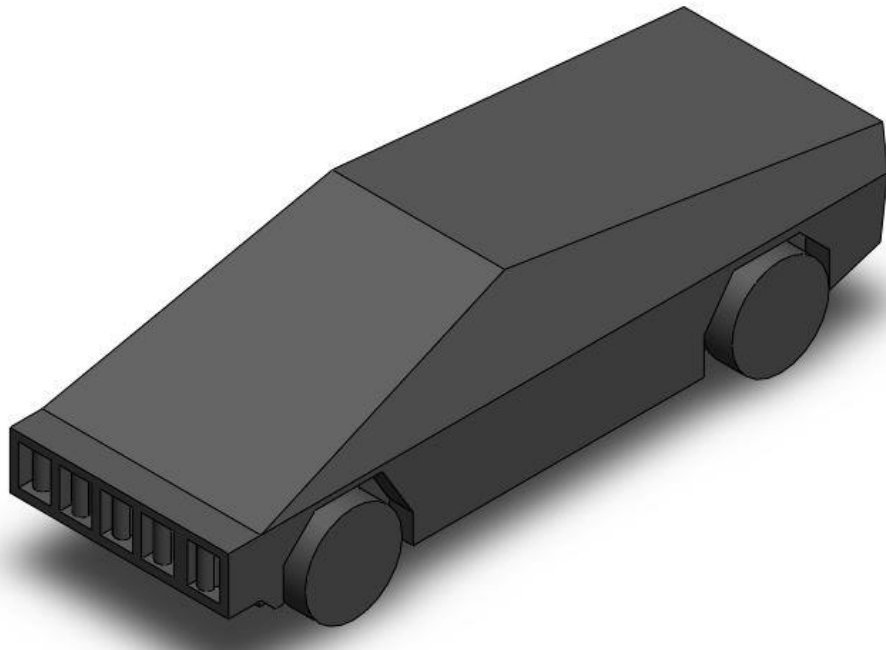


Figure 4.23 Design 3

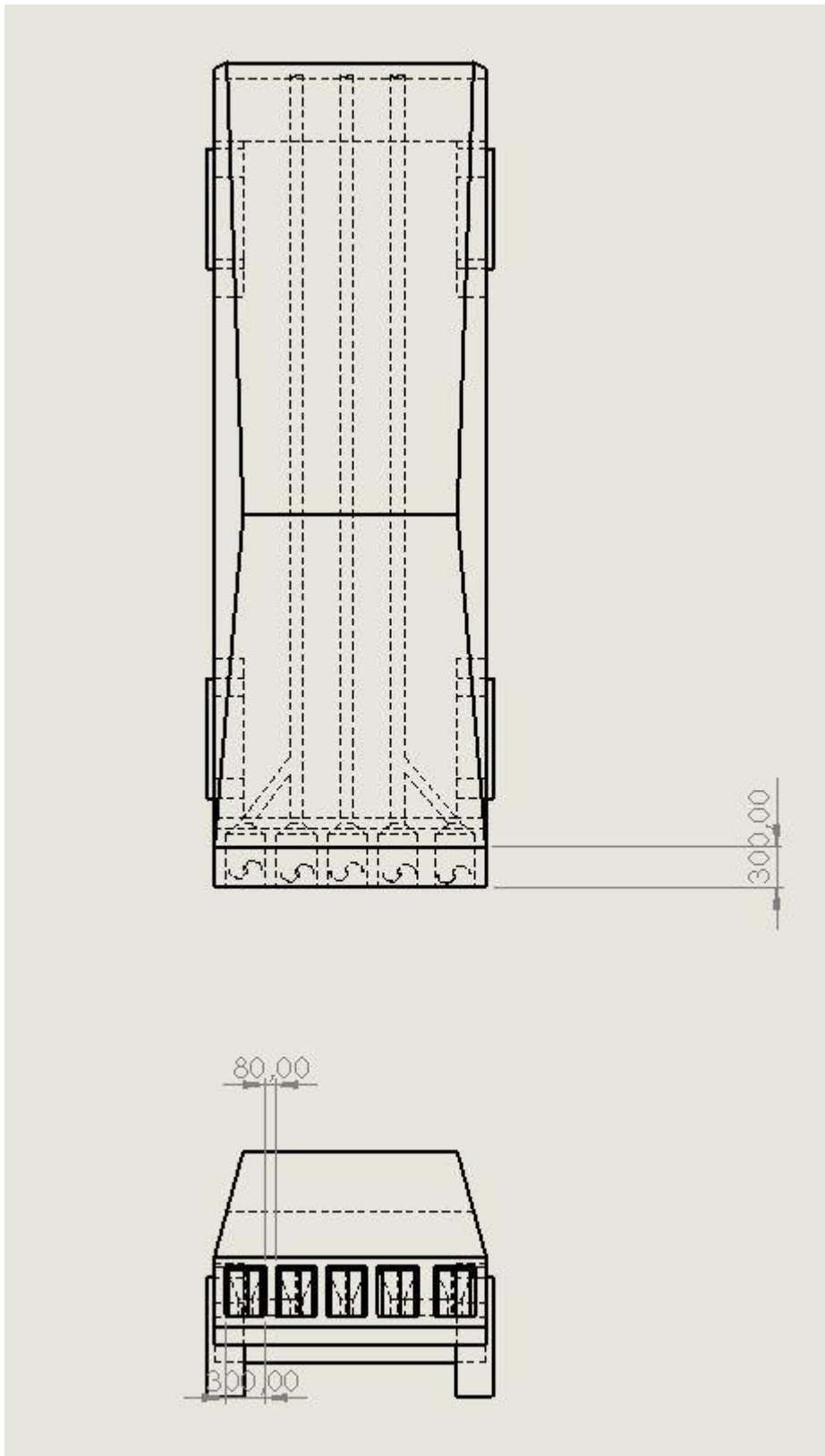


Figure 4.24 Technical Drawing of Design 3.

There will be 5 turbines with same geometries in previous designs.

Cells	Faces	Nodes
287746	592389	56573

Mesh Quality

Name	Type	Min Orthogonal Quality	Max Aspect Ratio
solid	Tet Cell	0.0063645002	172.42802

Orthogonal Quality

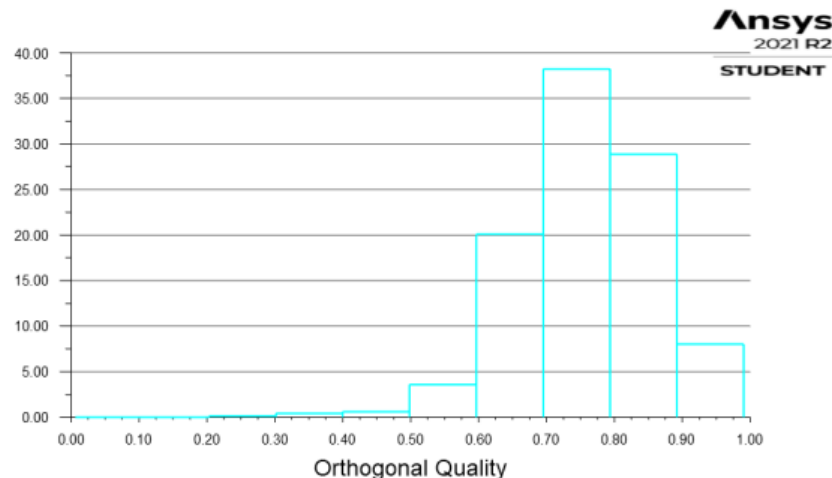


Figure 4.25 Quality of Meshing

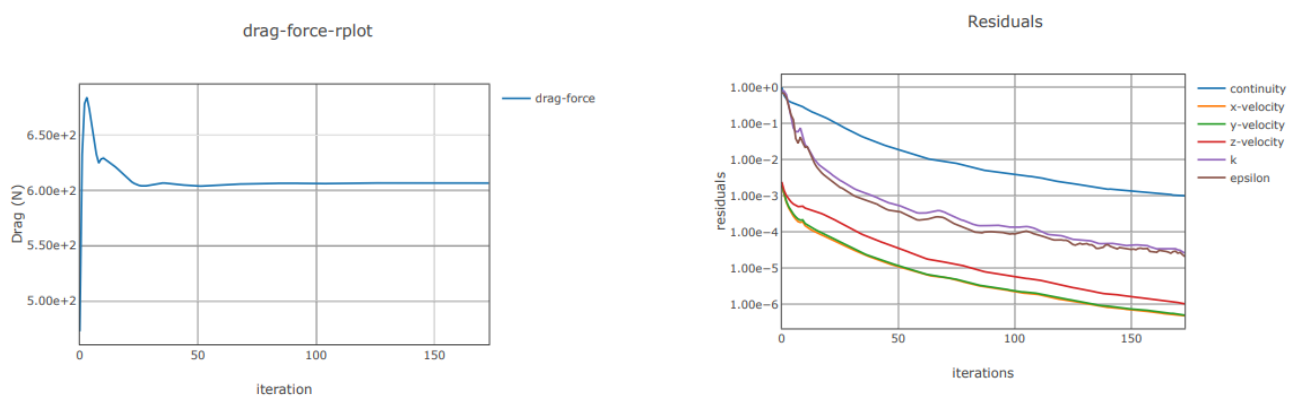


Figure 4.26 (a) Drag Force plot taken form ANSYS Report (b) Residuals

drag-force	606.7532 N
drag-coeff	0.455816

Figure 4.27 Drag force and drag coefficient of Design 3

It has decreased a remarkable amount of drag force with **28N**. It will be evaluated in Results Section 4.7.

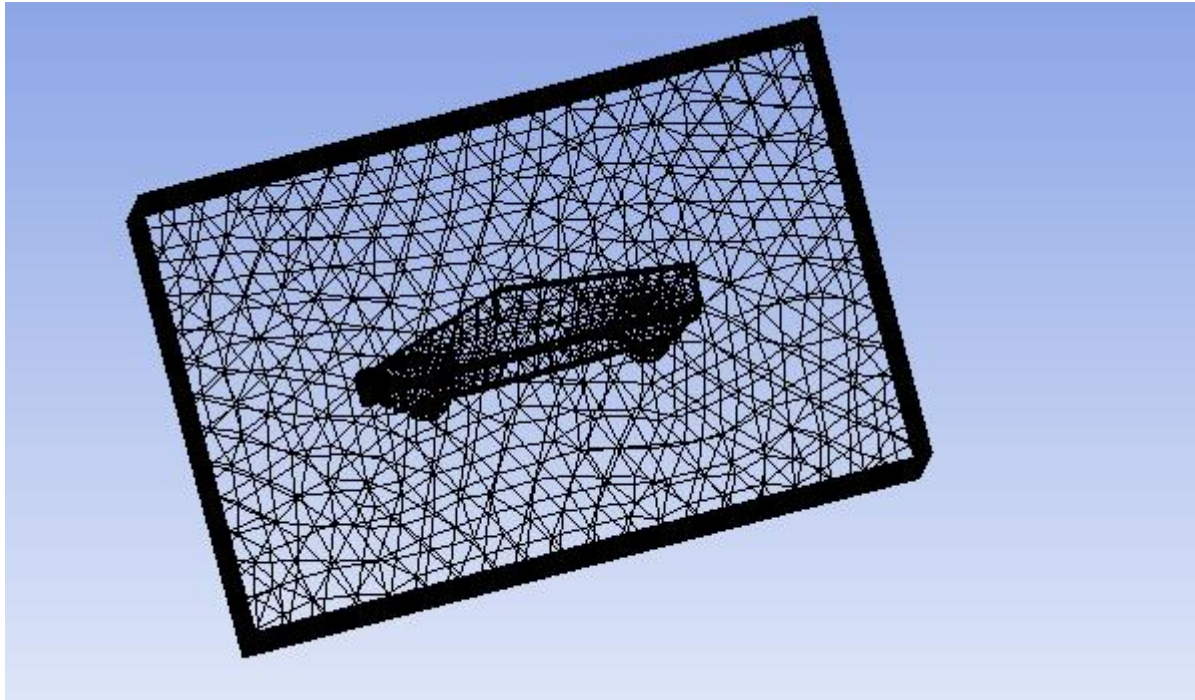


Table 4.2 Residuals for Design 3

	Value	Absolute Criteria	Convergence Status
continuity	0.0009974734	0.001	Converged
x-velocity	4.833866e-07	0.001	Converged
y-velocity	5.017511e-07	0.001	Converged
z-velocity	1.034039e-06	0.001	Converged
k	2.618582e-05	0.001	Converged
epsilon	2.098233e-05	0.001	Converged

x-y-z velocity, k and epsilon converged below 10e-03 and 10e-04 that is a criteria for CFD Analysis. Continuity residuals converged below 10e-03, that is not the best result to have for CFD analysis, it should be 10e-04. However, it is below 10e-03 that is still okay to have simulations.

4.5 Turbine Selection

In the wind turbine business there are basically two types of turbines to choose from, vertical axis wind turbines and horizontal axis wind turbines. They both have their advantages and disadvantages and the purpose of this article is to help you choose the right system for your application. Horizontal axis wind turbine dominate the majority of the wind industry. Horizontal axis means the rotating axis of the wind turbine is horizontal, or parallel with the ground. In big wind application, horizontal axis wind turbines are almost all you will ever see. However, in small wind and residential wind applications, vertical axis turbines have their place. The advantage of horizontal wind is that it is able to produce more electricity from a given amount of wind.

VAWT	HAWT
It works in turbulent airflow conditions.	It works in streamflow air conditions.
The major rotor shaft of vertical axis wind turbines fixes in a vertical direction.	The major shaft of the rotor of a horizontal axis wind turbine fixes in the horizontal direction.
It has low efficiency.	It has high efficiency.
Maintenance is easy.	Maintenance is difficult.
Drag is a major force.	Lift is a major force.
Yaw mechanism is not required.	Yaw mechanism is not required.

There are things to be considered when selecting the turbine. The turbine will be working in urban areas, so that it should be noiseless and directionfree to work. Two of the turbines are examined in previous section. It is noticed that VAWT's are not used commonly even though it has remarkable advantages. For a car, it is needed to have low maintenance cost for benefit of customer. A car running always encounters drag force and vertical axis wind turbines works with drag force. HAWTs seem more efficient but there will not be an enough space for HAWT. For the same size of turbine, VAWTs can be more efficient.

Savonius Turbines are widely used and it has been seen that it has great potential in usage. It has less noise and works with drag force as main component. It does not get affected by direction of wind. So that savonius turbine will be used with 2 blades. Savonius turbine is steady, less rotation and less noise.

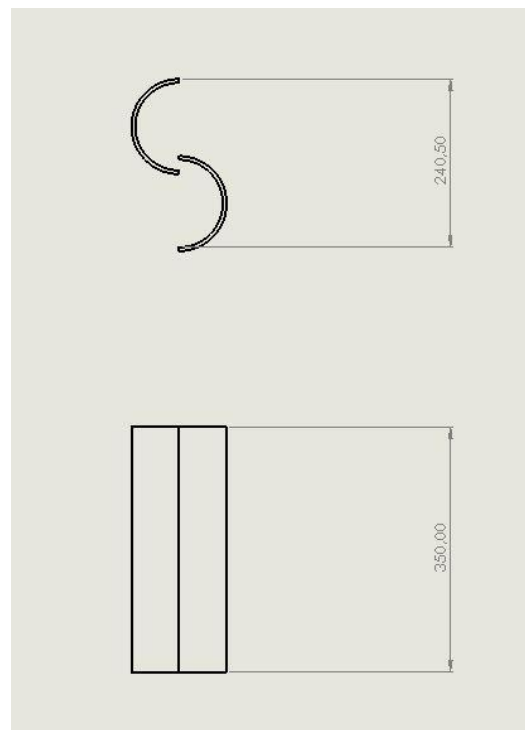
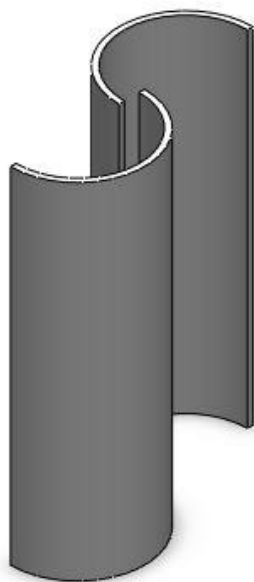


Figure 4.28 (a) 2-Blade Savonius turbine (b) Technical drawing

4.6 Drag Force-Energy Analyzes With Turbines

4.6.1 Drag Force on Design 1 With Turbines

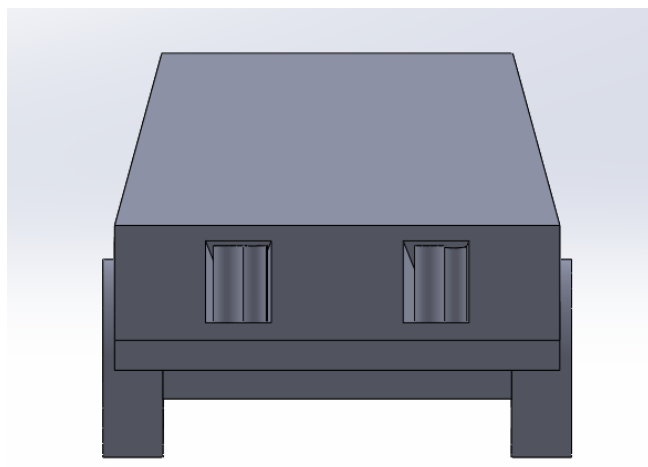


Figure 4.29 Wind Turbines set in front panel

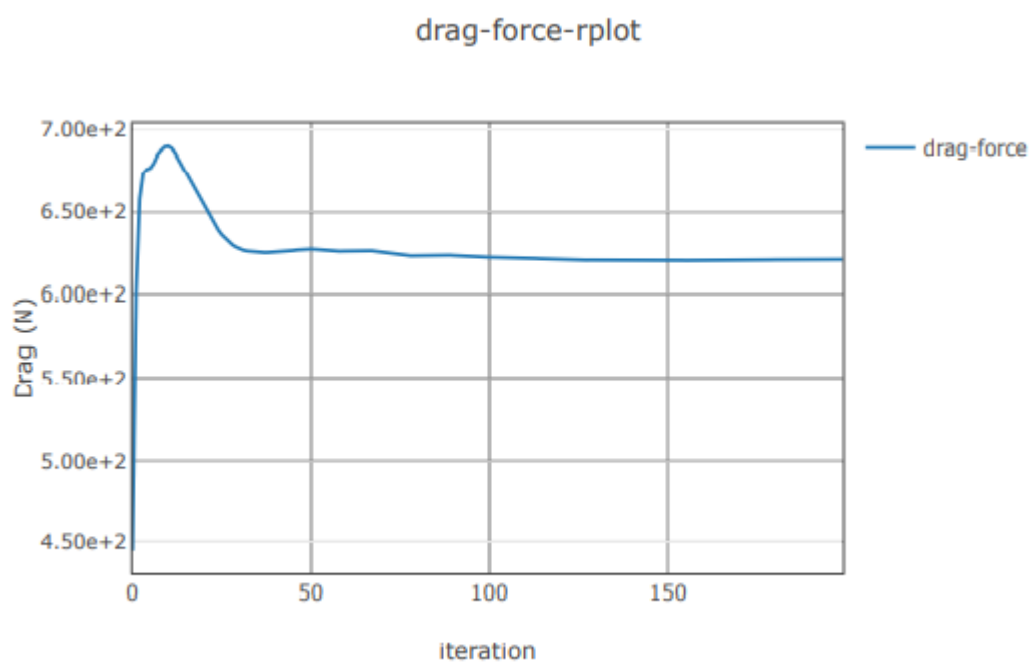
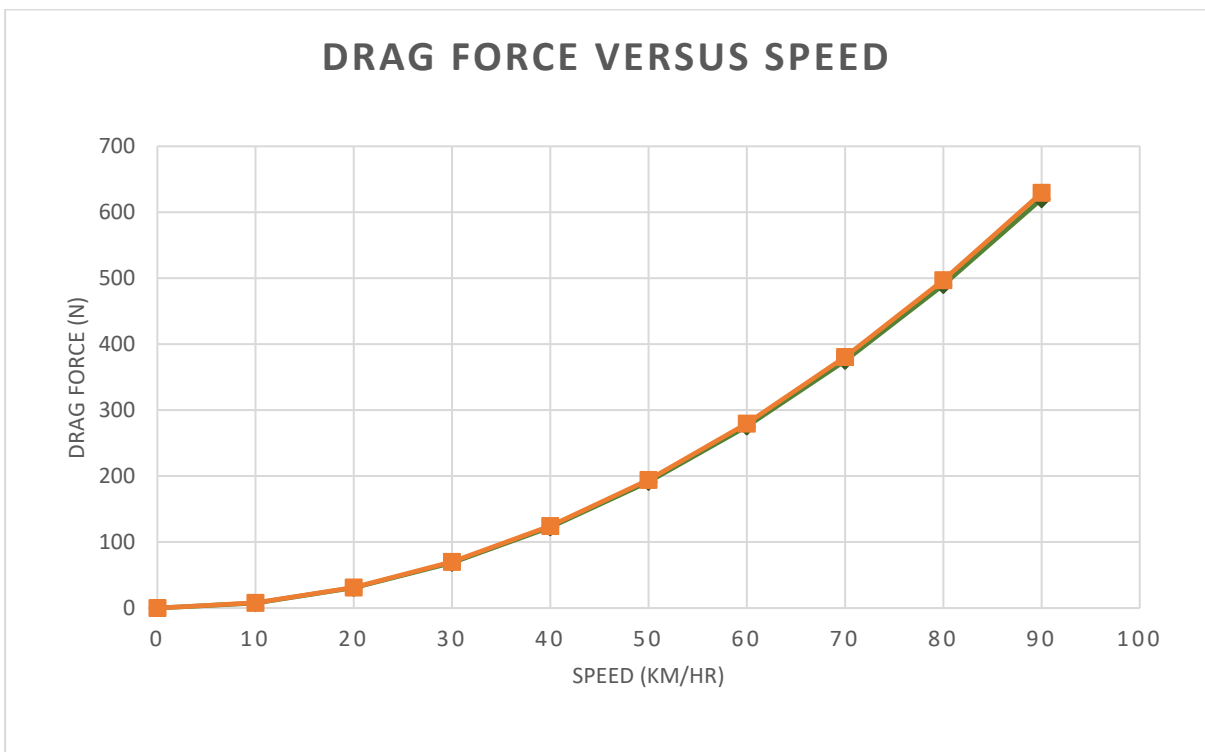


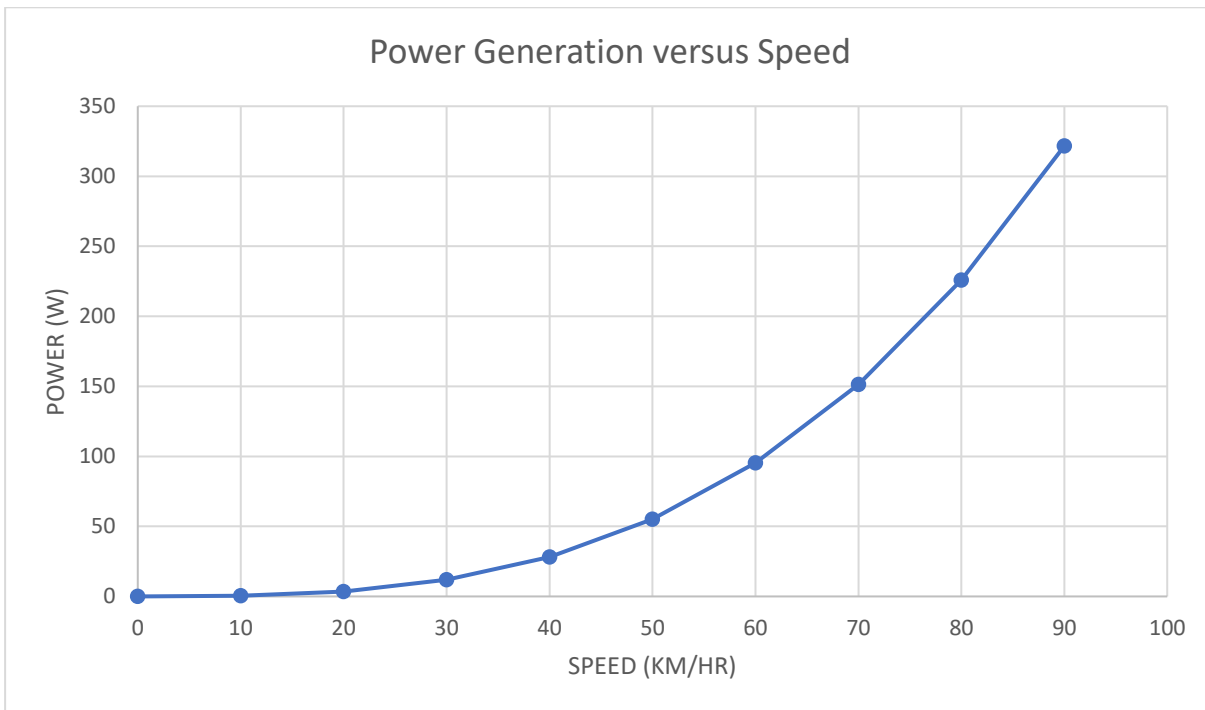
Figure 4.30 Drag force applied on design 1 with set of air ducts

drag-force	621.1189 N
drag-coeff	0.4666084

Figure 4.31 Drag force and coefficient simulated by ANSYS at 90km/hr speed



Drag forces are almost same. Design 1 has 8 N less drag force than simple vehicle has.



Power generation is **320W** at 90km/hr speed.

The performance ratio of turbine is taken as 0.2. The power generation is calculated theoretically using wind power formula. It will be used in next calculations also.

4.6.2 Drag Force on Design 2 With Turbines

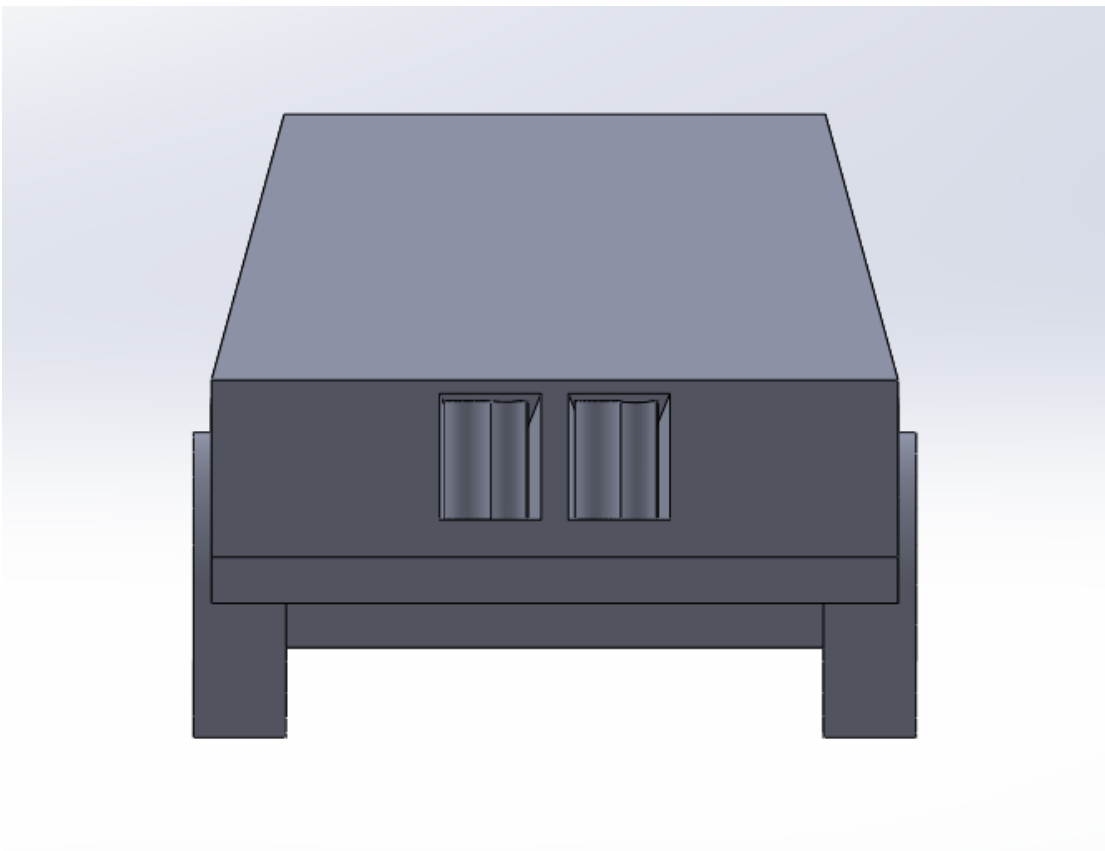


Figure 4.32 Wind Turbines set in middle of front panel

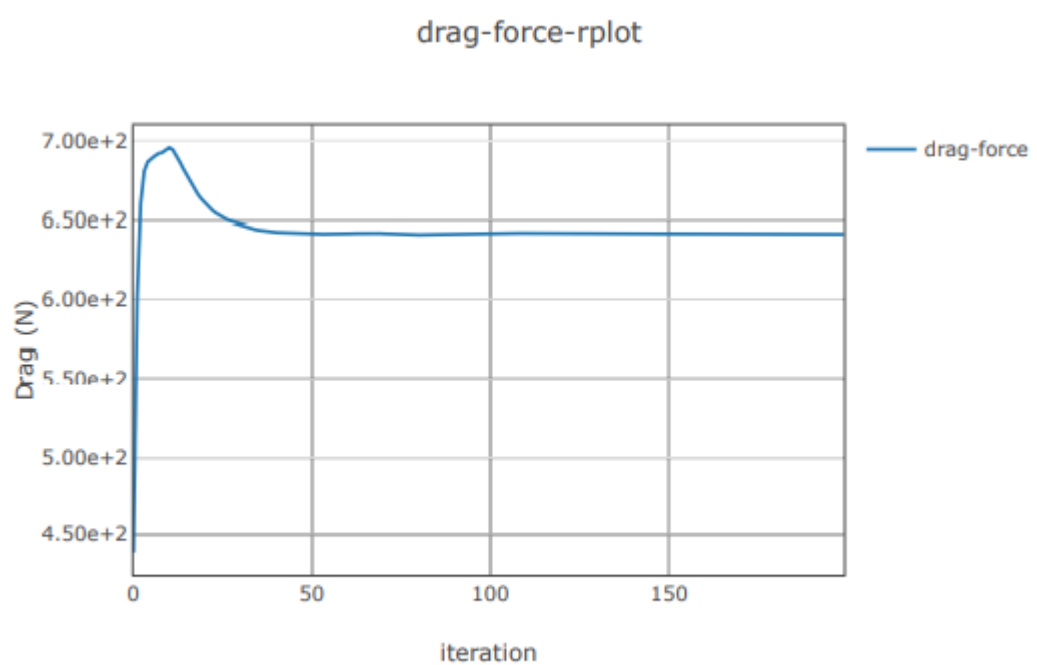
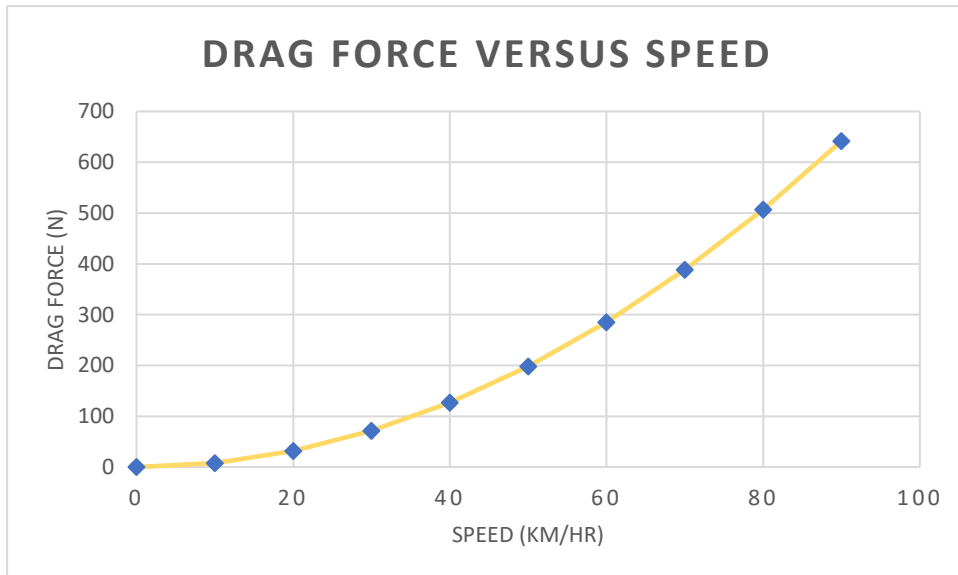


Figure 4.33 Drag force acting on vehicle body at 90 km/hr speed.

drag-force	641.9551 N
drag-coeff	0.4840894

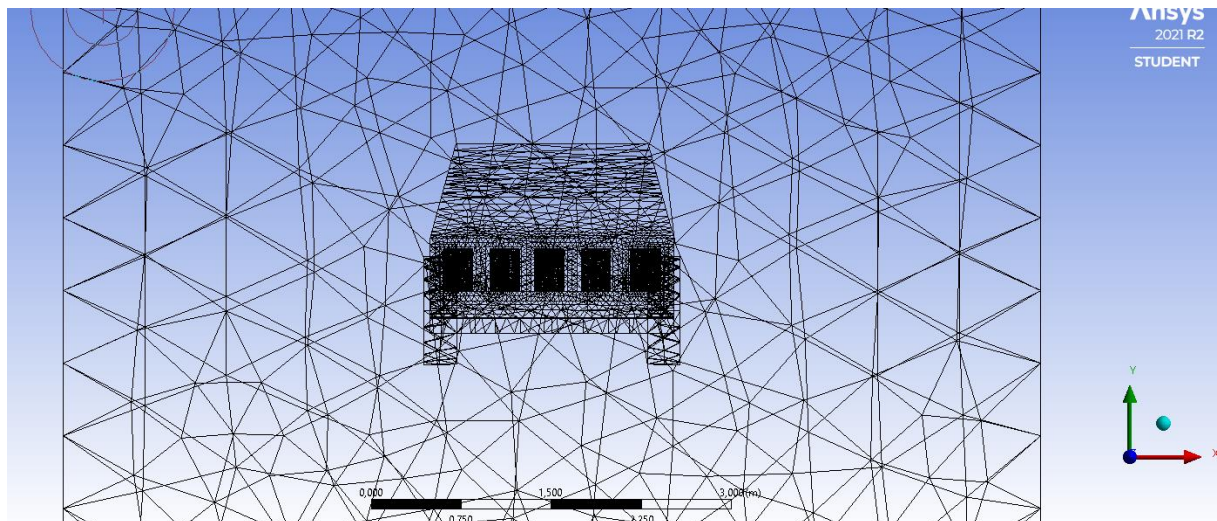
Figure 4.34 Drag force and coefficient simulated by ANSYS at 90km/hr speed



Drag force increased in this case. The increase in drag force is **12 N**. As drag force increased and power generation is same in both designs, design 2 is useless.

Power Output is same in both designs as same turbines are used.

4.6.3 Design 3



Models

Model	Settings
Space	3D
Time	Steady
Viscous	Standard k-epsilon turbulence model
Wall Treatment	Standard Wall Functions

Material Properties

— Fluid	
— air	
Density	1.225 kg/m ³
Cp (Specific Heat)	1006.43 J/(kg K)

Thermal Conductivity	0.0242 W/(m K)
Viscosity	1.7894e-05 kg/(m s)
Molecular Weight	28.966 kg/kmol
Thermal Expansion Coefficient	0
Speed of Sound	none
— Solid	
— aluminum	
Density	2719 kg/m ³
Cp (Specific Heat)	871 J/(kg K)
Thermal Conductivity	202.4 W/(m K)

Cell Zone Conditions

— Fluid	
— solid	
Material Name	air
Specify source terms?	no
Specify fixed values?	no
Frame Motion?	no
Laminar zone?	no
Porous zone?	no
3D Fan Zone?	no

Boundary Conditions

— Inlet	
— inlet	
Velocity Specification Method	Magnitude, Normal to Boundary
Reference Frame	Absolute
Velocity Magnitude [m/s]	25
Supersonic/Initial Gauge Pressure [Pa]	0
Turbulent Specification Method	Intensity and Viscosity Ratio
Turbulent Intensity [%]	5
Turbulent Viscosity Ratio	10
— Outlet	
— outlet	
Backflow Reference Frame	Absolute
Gauge Pressure [Pa]	0
Pressure Profile Multiplier	1
Backflow Direction Specification Method	Normal to Boundary
Turbulent Specification Method	Intensity and Viscosity Ratio
Backflow Turbulent Intensity [%]	5
Backflow Turbulent Viscosity Ratio	10
Backflow Pressure Specification	Total Pressure
Build artificial walls to prevent reverse flow?	no
Radial Equilibrium Pressure Distribution	no
Average Pressure Specification?	no

Specify targeted mass flow rate	no
— Wall	
— walls	
Wall Motion	Stationary Wall
Shear Boundary Condition	No Slip
Wall Roughness Height [m]	0
Wall Roughness Constant	0.5
— vehicle	
Wall Motion	Stationary Wall
Shear Boundary Condition	No Slip
Wall Roughness Height [m]	0
Wall Roughness Constant	0.5

Reference Values

Area	3.477252 m ²
Density	1.225001 kg/m ³
Enthalpy	0 J/kg
Length	5 m
Pressure	0 Pa
Temperature	288.16 K
Velocity	25 m/s
Viscosity	1.789402e-05 kg/(m s)
Ratio of Specific Heats	1.4
Yplus for Heat Tran. Coef.	300

Solver Settings

— Equations	
Flow	True
Turbulence	True
— Numerics	
Absolute Velocity Formulation	True
— Pseudo Transient Explicit Relaxation Factors	
Density	1
Body Forces	1
Turbulent Kinetic Energy	0.75
Turbulent Dissipation Rate	0.75
Turbulent Viscosity	1
Explicit Momentum	0.5
Explicit Pressure	0.5
— Pressure-Velocity Coupling	
Type	Coupled
Pseudo Transient	True
— Discretization Scheme	

Pressure	Second Order
Momentum	Second Order Upwind
Turbulent Kinetic Energy	First Order Upwind
Turbulent Dissipation Rate	First Order Upwind
— Solution Limits	
Minimum Absolute Pressure [Pa]	1
Maximum Absolute Pressure [Pa]	5e+10
Minimum Temperature [K]	1
Maximum Temperature [K]	5000
Minimum Turb. Kinetic Energy [m^2/s^2]	1e-14
Minimum Turb. Dissipation Rate [m^2/s^3]	1e-20
Maximum Turb. Viscosity Ratio	100000

Run Information

Number of Machines	1
Number of Cores	1
Case Read	3.72 seconds
Iteration	389.282 seconds
AMG	273.793 seconds
Virtual Current Memory	0.648754 GB
Virtual Peak Memory	0.877621 GB
Memory Per M Cell	1.7135

Solution Status

Iterations: 174

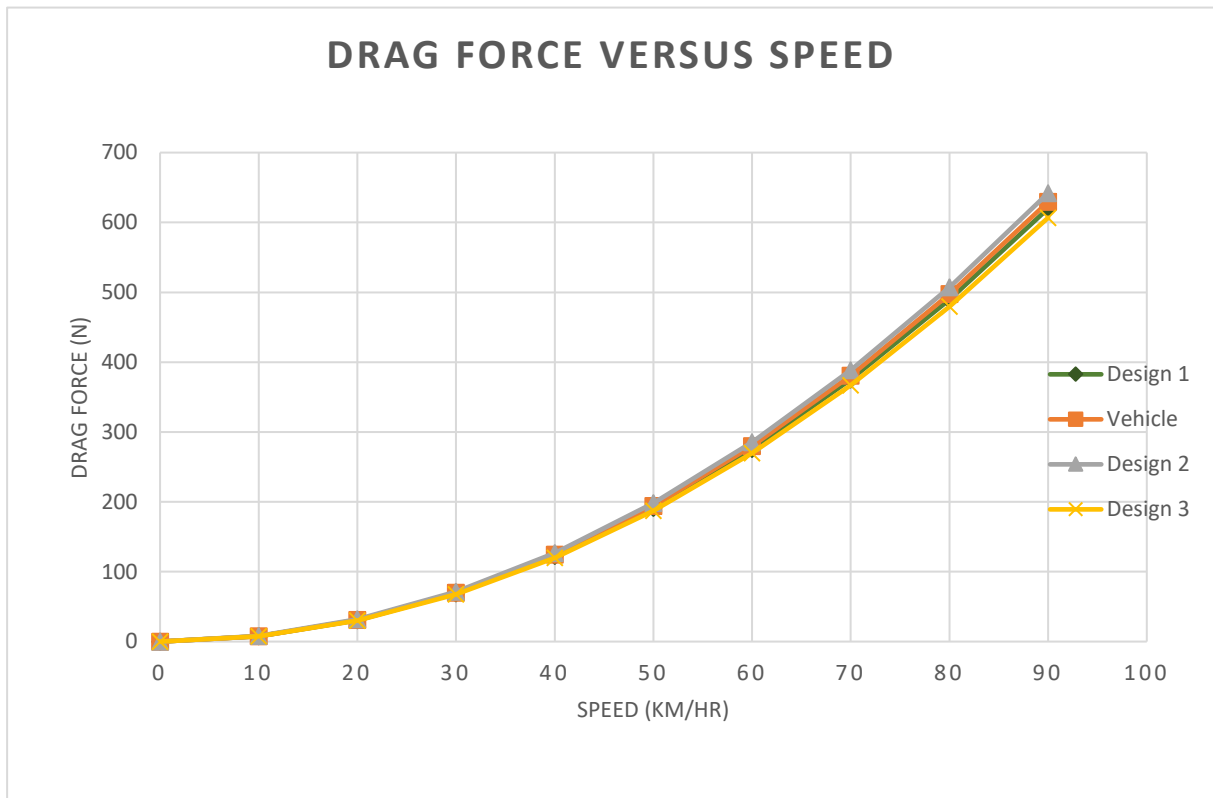
	Value	Absolute Criteria	Convergence Status
continuity	0.0009974734	0.001	Converged
x-velocity	4.833866e-07	0.001	Converged
y-velocity	5.017511e-07	0.001	Converged
z-velocity	1.034039e-06	0.001	Converged
k	2.618582e-05	0.001	Converged
epsilon	2.098233e-05	0.001	Converged

Solution Status

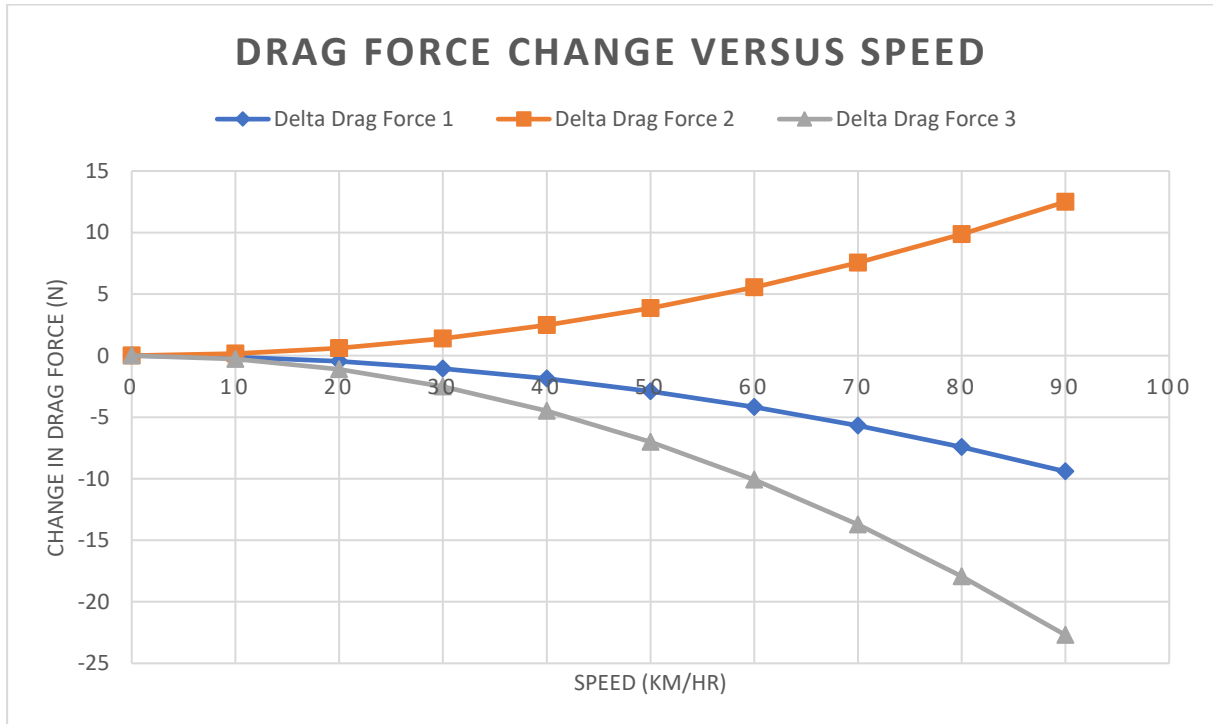
Iterations: 174

	Value	Absolute Criteria	Convergence Status
continuity	0.0009974734	0.001	Converged
x-velocity	4.833866e-07	0.001	Converged
y-velocity	5.017511e-07	0.001	Converged
z-velocity	1.034039e-06	0.001	Converged
k	2.618582e-05	0.001	Converged
epsilon	2.098233e-05	0.001	Converged

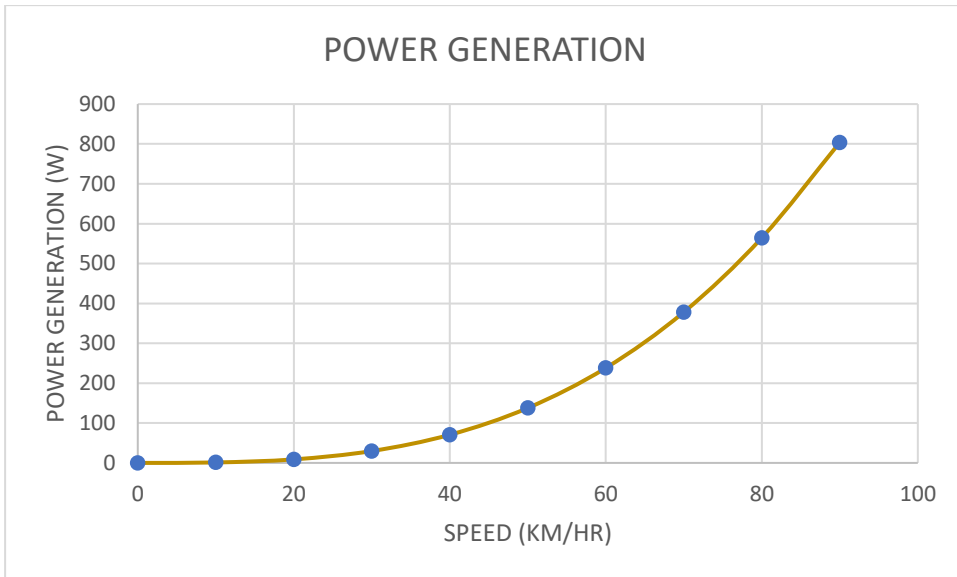
4.7 Results



It is seen above that the least drag force applied on vehicle is in Design 3.



The drag force change versus speed is shown above. Drag force decreased 22N at 90km/hr speed in Design 3. It also has more turbines, so that design 3 is chosen.



Power is generated with 800W at 90 km/hr.

	Vehicle	Drag Force(N)
1	CyberTruck	629
2	CyberTruck	621
3	CyberTruck with Design 2	641
4	CyberTruck with Design 3	606

Chapter 5

Cost Analysis and Conclusion

This chapter includes cost-design analysis and conclusion of the paper.

This chapter includes cost-design analysis and conclusion of the paper.

5.1 Cost-Design Analysis

Cost and Design is main factor when implementing a new function to any current technology. When it comes to vehicles, it's already high cost, especially EV's. With the help of this new function it can be beneficial for future usage to return the first cost. In previous chapter, it is calculated that turbine power is 800 at 90 km/h. Table below is taken from [tesla.com]

Model	Mass KG	Consumption	Fuel equiv. L/100KM	CO2 G/KM	CO2 G/KM*	CO2 G/KM**	Energy Efficiency
Model S 60	2045	18.1 kWh/100 km	2	0	26	137	A
Model S 70	2118	18.5 kWh/100 km	2	0	26	137	A
Model S 75	2188	18.5 kWh/100 km	2	0	26	137	A
Model X 75D	2523	20.8 kWh/100 km	2.3	0	29	137	A
Model S 90D	2309	18.9 kWh/100 km	2.1	0	26	137	A
Model S P90D	2357	20.0 kWh/100 km	2.2	0	28	137	A
Model S 100D	2376	18.9 kWh/100 km	2.1	0	26	137	A

* CO2 emissions from electricity supply

** Average value of all registered new cars in Switzerland

Real Energy Consumption Estimation		between 185 - 370 Wh/km	
City - Cold Weather *	256 Wh/km	City - Mild Weather *	185 Wh/km
Highway - Cold Weather *	370 Wh/km	Highway - Mild Weather *	299 Wh/km
Combined - Cold Weather *	308 Wh/km	Combined - Mild Weather *	238 Wh/km

Indication of real-world energy use in several situations. Cold weather: 'worst-case' based on -10°C and use of heating. Mild weather: 'best-case' based on 23°C and no use of A/C. For 'Highway' figures a constant speed of 110 km/h is assumed. The energy use will depend on speed, style of driving, climate and route conditions.

Tesla CyberTruck energy consumption is shown above. In turbine and geometry we selected, power output is 800W, at 90 km/h, it means that production is 8.89Wh/km, TESLA has 299 Wh/km. It is 2.97% of energy consumption.

Loads	Power(W)
Headlights(2)	120
Backlights	50
Hazard lights (4)	84
Power window(4)	120

The turbine can produce enough energy for lights and windows plus it can produce energy for A/C. So it can be considered by manufacturer to set such kind of air ducts.

5.2 Conclusion

The growing number of automobiles creates a tremendous demand for fossil fuels, which are rapidly depleting. Developing a wind-powered car will be environmentally benign, as it will use no fossil fuel and will harness energy from the atmosphere. The wind-powered vehicle is designed to take advantage of non-conventional energy sources that are abundant in nature. There are a variety of ways to harvest such energies in our daily lives, and this is only one of them. A wind turbine is utilized for this purpose, which gathers and stores energy in a battery, which helps to extend the vehicle's runtime and also helps to charge the vehicle. Cost-effectiveness, environmental friendliness, and free energy conservation are all advantages that can be incorporated. The vehicle's present weight is a worry, as it limits the vehicle's speed. The vehicle can be employed in a variety of industries where fossil fuels are expensive and cities are struggling to reduce their carbon imprint. Electric automobiles that can charge on the

go may appear in the future, and wind power will be one of them. We may deduce from the graphs, Speed of the blade vs. Power, that the power generated by the turbine increases as the blade speed increases. The graph of blade speed vs. voltage indicates that as the blade speed increases, the voltage produced by the turbine increases. The graph of blade speed vs. current demonstrates that the current produced by the turbine grows as the blade speed increases. The relationship between linear velocity and blade speed shows that the blade's speed increases as the vehicle's linear velocity increases. Some of the advantages this vehicle has are that it uses sustainable energy as fuel, which does not contaminate the environment, that it conserves energy, which is free and abundant, and that it can be used in daily life, and that it is environmentally friendly. Compared to other electric cars, it is less expensive or more cost effective, and unlike solar vehicles, it can create energy at any time of day. The design of a wind power harvester was proposed and assessed in this article to promote optimal operation. The aerodynamic drag and air speed characteristics around the vehicle with a wind turbine framework were studied statistically. A Fluent module of ANSYS software was used to simulate the vehicle model in order to consider the wind stream signature around the vehicle body and determine the vehicle's drag power at a certain speed.

References

Ms. NannooriSwathi, Mr. Prof.J.Nagaraju “Fabrication of Advanced Wind Powered Augumented Electric Vehicle” International Journal and Magazine of Engineering, Technology, Management and Research, Vol.2, July 2015, ISSN No. 2348-4845

Dyachuk, E. (2015). Aerodynamics of Vertical Axis Wind Turbines - *Development of Simulation Tools and Experiments*. Retrieved from
<http://urn.kb.se/resolve?urn=urn:nbn:se:uu:diva-260573>

Ferziger, J. H., Peric, M., & Leonard, A. (1997). *Computational Methods for Fluid Dynamics*. Physics Today. <https://doi.org/10.1063/1.881751>

Froude, R. (1889). On the part played in the operation of propulsion differences in fluid pressure. Trans RINA 30, 390–405.

Hellsten, A. (1997). Some Improvements in Menter ’s k- ω SST Turbulence Model.

J. D. Anderson, J. (2009). Governing Equations of Fluid Dynamics. Computational Fluid Dynamics, 15–51. https://doi.org/10.1007/978-3-540-85056-4_2

Jensen, B. B. B. (2007). Numerical study of influence of inlet turbulence parameters on turbulence intensity in the flow domain: incompressible flow in pipe system. Proc. IMechE Vol. 221 Part E: J. Process Mechanical Engineering, 221, 177– 185.

Kacprzak, K., Liskiewicz, G., & Sobczak, K. (2013). Numerical investigation of conventional and modified Savonius wind turbines. Renewable Energy, 60, 578–585. <https://doi.org/10.1016/j.renene.2013.06.009>

Kundu, P. K., Cohen, I. M., & Dowling, D. R. (2016). FLUID MECHANICS SIXTH EDITION. Fluid Mechanics. <https://doi.org/10.1016/B978-0-12-405935-1.01001-7>

Leblanc, B. P., & Ferreira, C. S. (2018). Experimental Determination of Thrust Loading of a 2-Bladed Vertical Axis Wind Turbine. Journal of Physics: Conference Series, 1037(2). <https://doi.org/10.1088/1742-6596/1037/2/022043>

Linton, D., Barakos, G., Widjaja, R., & Thornbern, B. (2017). A new actuator surface model with improved wake model for CFD simulations of rotorcraft. In Proceeding of the 73rd Annual Forum and Technology Display of the American Helicopter Society. Fort Worth, TX, USA,.

- Martínez-Tossas, L. A., Churchfield, M. J., & Meneveau, C. (2015). Optimal smoothing length scale for actuator line models of wind turbine blades. *Wind Energy*. <https://doi.org/10.1002/we>
- N.S. Hanamapure, Ajit B. Bachche “Wind Energy Utilization of Generation of Electricity on an Automobile” International Journal of Engineering and Innovating Technology, Vol.2, Issue 7, January 2013
- Price, T. J. (2005). James Blyth — Britain’s First Modern Wind Power Pioneer. *Wind Engineering*, 29(3), 191–200. <https://doi.org/10.1260/030952405774354921>
- Xie, X.; Wang, Q. A mathematical model for piezoelectric ring energy harvesting technology from vehicle tires. *Int. J. Eng. Sci.* 2015, 94, 113–127
- Ochieng, R.; Ochieng, R. Analysis of the betz criterion in wind turbine power modelling by use of “variational principle (method)” in the power equation. *Int. J. Energy, Environ. Econ.*
- Fotso, B.M.; Nguefack, C.F.; Talawo, R.C.; Fogue, M. Aerodynamic analysis of an electric vehicle equipped with horizontal axis savonius wind turbines. *Int. J. Recent Trends Eng. Res. IJRTTER* 2019, 5, 17–26
- Muller, S., Deicke, M., and De Doncker, R. W. 2002. Doubly fed induction generator systems for wind turbines. *IEEE Industry Applications Magazine*, 8(3), pp. 26-33.
- Tran, D. 2011. Vehicle Air Turbine. U.S. Patent Application 13/210,597.
- Schär, C. 1993. A generalization of Bernoulli's theorem. *Journal of the atmospheric sciences*, 50(10), pp. 1437- 1443.
- Ripley, P. W. 2013. Wind turbine for electric car. U.S. Patent No. 8,513,828. Washington, DC: U.S. Patent and Trademark Office.
- Prakash, R., and Bhat, I. K. 2009. Energy, economics and environmental impacts of renewable energy systems. *Renewable and Sustainable Energy Reviews*, 13(9), pp. 2716-2721.
- Runchal AK. (1969). Transport processes in steady two-dimensional separated flows. Ph.D. Thesis. Imperial College of Science and Technology, London, UK.
- Salter, S. H., & Taylor, J. R. M. (2007). Vertical-axis tidal-current generators and the Pentland Firth. *Proceedings of the Institution of Mechanical Engineers, Part A: Journal of Power and Energy*. <https://doi.org/10.1243/09576509JPE295>
- Savonius, S. J. (1929). Rotor adapted to be driven by wind or flowing water. US Patent 1,697,574.

Schwarze, R., & Obermeier, F. (2006). Performance and limitations of the unsteady RANS approach. PAMM · Proc. Appl. Math. Mech, 6(1), 577–578.

<https://doi.org/10.1002/pamm.200610>

Strickland, J. (1975). The Darrieus Turbine, A Performance Prediction Method Using Multiple Stream Tubes. Sandia Laboratories, SAND. <https://doi.org/SAND75-0431>

https://airshaper.com/cases/tesla-cybertruck-aerodynamics